



The Carnegie-Chicago Hubble Program. VIII. An Independent Determination of the Hubble Constant Based on the Tip of the Red Giant Branch*

Wendy L. Freedman¹ , Barry F. Madore² , Dylan Hatt¹ , Taylor J. Hoyt¹ , In Sung Jang³ , Rachael L. Beaton⁴ , Christopher R. Burns² , Myung Gyoong Lee⁵ , Andrew J. Monson⁶, Jillian R. Neeley⁷ , M. M. Phillips⁸ , Jeffrey A. Rich² , and Mark Seibert²

¹ Department of Astronomy & Astrophysics, University of Chicago, 5640 South Ellis Avenue, Chicago, IL 60637, USA; wfreedman@uchicago.edu

² The Observatories of the Carnegie Institution for Science, 813 Santa Barbara Street, Pasadena, CA 91101, USA

³ Leibniz-Institut für Astrophysik Potsdam, D-14482 Potsdam, Germany

⁴ Department of Astrophysical Sciences, Princeton University, 4 Ivy Lane, Princeton, NJ 08544, USA

⁵ Department of Physics & Astronomy, Seoul National University, Gwanak-gu, Seoul 151-742, Republic of Korea

⁶ Department of Astronomy & Astrophysics, Pennsylvania State University, 525 Davey Lab, University Park, PA 16802, USA

⁷ Department of Physics, Florida Atlantic University, 777 Glades Road, Boca Raton, FL 33431, USA

⁸ Carnegie Institution of Washington, Las Campanas Observatory, Casilla 601, Chile

Received 2019 April 25; revised 2019 June 22; accepted 2019 July 3; published 2019 August 29

Abstract

We present a new and independent determination of the local value of the Hubble constant based on a calibration of the tip of the red giant branch (TRGB) applied to Type Ia supernovae (SNe Ia). We find a value of $H_0 = 69.8 \pm 0.8 (\pm 1.1 \text{ stat}) \pm 1.7 (\pm 2.4 \text{ sys}) \text{ km s}^{-1} \text{ Mpc}^{-1}$. The TRGB method is both precise and accurate and is parallel to but independent of the Cepheid distance scale. Our value sits midway in the range defined by the current Hubble tension. It agrees at the 1.2σ level with that of the Planck Collaboration et al. estimate and at the 1.7σ level with the *Hubble Space Telescope (HST) SHoES* measurement of H_0 based on the Cepheid distance scale. The TRGB distances have been measured using deep *HST* Advanced Camera for Surveys imaging of galaxy halos. The zero-point of the TRGB calibration is set with a distance modulus to the Large Magellanic Cloud of $18.477 \pm 0.004 \text{ (stat)} \pm 0.020 \text{ (sys)} \text{ mag}$, based on measurement of 20 late-type detached eclipsing binary stars, combined with an *HST* parallax calibration of a $3.6 \mu\text{m}$ Cepheid Leavitt law based on *Spitzer* observations. We anchor the TRGB distances to galaxies that extend our measurement into the Hubble flow using the recently completed Carnegie Supernova Project I (CSP-I) sample containing about 100 well-observed SNe Ia. There are several advantages of halo TRGB distance measurements relative to Cepheid variables; these include low halo reddening, minimal effects of crowding or blending of the photometry, only a shallow (calibrated) sensitivity to metallicity in the I band, and no need for multiple epochs of observations or concerns of different slopes with period. In addition, the host masses of our TRGB host-galaxy sample are higher, on average, than those of the Cepheid sample, better matching the range of host-galaxy masses in the CSP-I distant sample and reducing potential systematic effects in the SNe Ia measurements.

Key words: cosmological parameters – distance scale – galaxies: distances and redshifts – stars: low-mass – stars: Population II

1. Introduction

The Hubble constant (H_0), which parameterizes the current expansion rate of the universe, plays a critical role in cosmology by setting the absolute size scale for the universe. In recent decades, remarkable progress has been made in improving the accuracy (by identifying and decreasing the systematic errors) in measurements of H_0 . From a factor of 2 uncertainty in measuring extragalactic distances only a few decades ago, a value of H_0 measured to 10% was made possible with the availability of the *Hubble Space Telescope (HST)*; Freedman et al. 2001), and more recently, the

uncertainties have been reduced to less than 5% by a number of investigations (e.g., Freedman & Madore 2010; Freedman et al. 2012; Riess et al. 2016; Suyu et al. 2017).

Recently, a diverse set of increasingly precise measurements have led to convergence on a standard cosmology: a model of the universe whose energy + matter density is dominated by dark energy (in the form of a cosmological constant, Λ) and cold dark matter (CDM). This concordance Λ CDM model is consistent with a wide array of independent observations including, but not limited to, measurement of anisotropies in the temperature and polarization of the cosmic microwave background (CMB; e.g., Bennett et al. 2013; Planck Collaboration et al. 2018), fluctuations in the density of baryonic matter or baryonic acoustic oscillations (BAOs; e.g., Cole et al. 2005; Eisenstein et al. 2005; Aubourg et al. 2015; Alam et al. 2017), and observations of the magnitude–redshift relation for high-redshift Type Ia supernovae (SNe Ia; e.g., Riess et al. 1998; Perlmutter et al. 1999; Betoule et al. 2014; Scolnic et al. 2018).

The temperature and polarization anisotropy spectra for the Planck Collaboration et al. (2018) data are extremely well fit by a six-parameter-only Λ CDM model. While some parameters

* Based on observations made with the NASA/ESA *Hubble Space Telescope*, obtained at the Space Telescope Science Institute, which is operated by the Association of Universities for Research in Astronomy, Inc., under NASA contract NAS 5-26555. These observations are associated with program Nos. 13472 and 13691.



Original content from this work may be used under the terms of the [Creative Commons Attribution 3.0 licence](#). Any further distribution of this work must maintain attribution to the author(s) and the title of the work, journal citation and DOI.

are derived from the CMB measurements with extremely high precision (e.g., the angular size of the sound horizon, which is measured to an extraordinary precision of $\pm 0.03\%$; Planck Collaboration et al. 2018), the CMB measurements themselves do not give a direct measure of H_0 . They provide instead an indirect constraint—with a very small uncertainty—but only under the assumption of this six-parameter cosmological model. Assuming this standard Λ CDM model, the Planck Collaboration inferred a value of the Hubble constant of $67.4 \pm 0.5 \text{ km s}^{-1} \text{ Mpc}^{-1}$.

This CMB-modeled value of H_0 stands in stark contrast to two decades of (systematically larger) determinations of the local value of H_0 (e.g., Freedman et al. 2001, 2012; Riess et al. 2011, 2016; Sorce et al. 2013; Suyu et al. 2017; Birrer et al. 2018; Burns et al. 2018). The determination of Riess et al. (2019), $H_0 = 74.03 \pm 1.42 \text{ km s}^{-1} \text{ Mpc}^{-1}$, is $+6.6 \text{ km s}^{-1} \text{ Mpc}^{-1}$ larger and 4.4σ discrepant with the above value of $67.4 \pm 0.5 \text{ km s}^{-1} \text{ Mpc}^{-1}$ quoted by Planck Collaboration et al. (2018). It represents a 10% difference between the two distance scales. Moreover, the significance of this divergence has been increasing with time. While the locally determined value of H_0 has not changed appreciably (the value of the Hubble constant determined by the *HST* Key Project nearly 20 yr ago was $72 \pm 8 \text{ km s}^{-1} \text{ Mpc}^{-1}$), both the precision and the accuracy of the local measurements have increased considerably, with the quoted errors dropping from 10% in 2001 to less than 3% in 2018. The Planck errors have been consistently smaller and stable, at the 2% level when they were first reported in 2014 and now $< 1\%$ in 2018.

An additional means of determining H_0 is based on measurements of fluctuations in the matter density resulting from the imprint of BAO at recombination (Aubourg et al. 2015; Alam et al. 2017; Macaulay et al. 2018). Applying an “inverse” distance ladder approach, the absolute calibration for the distance scale (or, equivalently, the absolute magnitude calibration of SNe Ia) is set by adopting a sound horizon scale for the CMB (and not from Cepheids or the tip of the red giant branch (TRGB), as in the local universe measurements). The sound horizon, r_s , depends on early-time physics, requiring knowledge of the density and equation-of-state parameters of different species in the early universe. Adopting a sound horizon scale of $r_s = 147.05 \pm 0.30 \text{ Mpc}$ ($\pm 0.2\%$) (Planck Collaboration et al. 2018), Macaulay et al. most recently obtained a value of $H_0 = 67.77 \pm 1.30 \text{ km s}^{-1} \text{ Mpc}^{-1}$ based on a sample of 329 SN Ia and BAO measurements from the Dark Energy Survey. In this analysis, the relative SN Ia distance measurements serve to extrapolate the (also relative) BAO measurements made at larger redshifts down to redshift $z = 0$. Therefore, the BAO calibration of H_0 is not completely independent of the Planck measurement, since both H_0 determinations are based on the standard Λ CDM model and its adopted value of the sound horizon scale. However, the combination of BAO, CMB, and SN Ia measurements provides a very powerful constraint on the shape of the distance-redshift relation from $z = 1100$ to the present day, limiting possible variations in $H(z)$ that might potentially alleviate some of the current tension in H_0 .

1.1. Possible Sources of the Tension in H_0

Given the increasing tension with the Planck results over time, it is critically important to enumerate and assess quantitatively the impact of all systematic uncertainties that

may still be affecting one (or more) of these methods and models (Freedman 2017). The stakes for resolving this tension are particularly high: the persistent tension may be signaling fundamental physics beyond the baseline Λ CDM standard model.

Many possible explanations for the $6 \text{ km s}^{-1} \text{ Mpc}^{-1}$ discrepancy have been considered in the recent literature, but to date, all have been found lacking. Two long-standing questions have been discussed extensively and resolved: (1) the issue of whether we live in a Local Bubble and (2) the effects of weak lensing on the SN Ia measurements.

The question of whether or not we live in an underdense local void or bubble has recently been readdressed by Wu & Huterer (2017), Hoscheit & Barger (2018), and D’Arcy Kenworthy et al. (2019, and references therein). They concluded, in agreement with previous studies, that an effect of this kind is too small to explain the magnitude of the observed tension. In their detailed numerical simulations, Wu & Huterer found that the typical sample variance in H_0 in the local universe amounts to $\pm 0.31 \text{ km s}^{-1} \text{ Mpc}^{-1}$, more than an order of magnitude smaller than the observed discrepancy, and they further concluded that the existence of a void of the required size is of negligible probability in a Λ CDM model.

The second long-standing question is whether an effect due to weak lensing could be systematically affecting the dispersion of SN Ia magnitudes as distant SNe Ia are lensed by matter along the line of sight (e.g., Frieman 1996; Holz 1998). The SNe Ia will be magnified in brightness when the lensing convergence is positive and then demagnified when it is negative. The effect will increase with increasing redshift, as longer path lengths are traversed. Once more, however, this effect is found to be far too small to explain the measured H_0 difference (see, for example, Smith et al. 2014, and references therein). While the expected lensing effects are seen to modestly increase the scatter in the observed Hubble diagram, they do not contribute in a systematic way to the measurement of H_0 .

If the tension persists and cannot be attributed to a known astrophysical effect or systematic error, what are the alternatives? The observed tension could be signaling additional fundamental new physics, beyond either the current astronomers’ six-parameter standard Λ CDM model or the physicists’ standard model of particle physics. At present, the dominant components of the standard model of cosmology are dark energy and dark matter, neither of which has a firm theoretical foundation. Simple examples of physics beyond the standard Λ CDM model could include evolution of the dark energy equation of state or an increase in the energy density of radiation in the early universe, which would modify the early expansion history of the universe (e.g., Bernal et al. 2016; Mörtzell & Dhawan 2018). At present, however, these types of late-time modifications do not lead to a clear improvement in the cosmological model (see, for example Planck Collaboration et al. 2016, 2018, and references therein).

Indeed, the simplest proposed changes (for example, increasing the number of relativistic species or changing the equation of state for dark energy) worsen the model fit to the CMB anisotropy spectra and lead to conflicts with measurements from BAO, weak lensing, SN Ia, and/or big bang nucleosynthesis (BBN) measurements (Planck Collaboration et al. 2018). More recently, there has been renewed attention to exploring additional new early-time physics operating prior to

recombination (e.g., Karwal & Kamionkowski 2016; Poulin et al. 2018; Agrawal et al. 2019). These early-universe models can provide a fit to the measured CMB spectra, although some fine-tuning is required to preserve the CMB fits at late times. Alternatively, non-Gaussian primordial fluctuations in the CMB resulting from long-wavelength (super-CMB) modes may offer a means of explaining some of the observed tension (Adhikari & Huterer 2019). It remains the case that resolving a $+6 \text{ km s}^{-1} \text{ Mpc}^{-1}$ difference in H_0 presents a considerable challenge for theory. Even with these nontrivial theoretical challenges, a reasonable general question remains: do we yet have a complete cosmological model with an understanding of early-universe physics? The issue remains open at present. With a nod to Carl Sagan, claims for exotic new physics beyond the standard model demand independent and “extraordinary evidence.”

1.2. Improving the Local Measurements of H_0

The strongest evidence at present for a high value of H_0 ($>70 \text{ km s}^{-1} \text{ Mpc}^{-1}$) rests on an empirical Cepheid calibration of the distances to galaxies hosting SNe Ia (e.g., Riess et al. 2016, 2019; hereafter *SHoES*). Several reanalyses of the earlier *SHoES* data (e.g., Efstathiou 2014; Feeney et al. 2017; Follin & Knox 2017; Zhang et al. 2017) find statistical consistency with the original analysis of *SHoES*; however, in all of these cases, the starting point is the same set of reduced data for the Cepheids as previously analyzed and published as part of the *SHoES* program.⁹ If, for example, there are as-yet-unrecognized systematic errors in the published Cepheid photometry, all follow-up studies would be blind to them. An accurate determination of H_0 rests squarely on an accurate determination of the zero-point of the extragalactic distance scale. This situation argues strongly for having an alternative method that is completely independent of the Cepheids, capable of providing its own absolute calibration for local measurements of H_0 .

The Carnegie-Chicago Hubble Program (CCHP) has been specifically designed to provide this alternative route to the calibration of SNe Ia and thereby provide an independent determination of H_0 via measurement of the TRGB in nearby galaxies.¹⁰ This method has a precision equal to or better than the Cepheid period–luminosity relation (the Leavitt law), and its current accuracy is also comparable. In five recent papers, we have presented TRGB distances to nine galaxies that are host to 11 SNe Ia, discussed the calibration of the data, and undertaken extensive artificial star tests and error analyses: NGC 1365 (Jang et al. 2018, hereafter Paper III); NGC 4424, NGC 4526, and NGC 4536 (Hatt et al. 2018a, hereafter Paper IV); NGC 1316 and NGC 1448 (Hatt et al. 2018b, hereafter Paper V); M66 and M96 (Hoyt et al. 2019, hereafter Paper VI); and M101 (Beaton 2019, hereafter Paper VII). We have also undertaken a detailed comparison of the Cepheid, RR Lyrae, and TRGB distances within the nearby Local Group galaxy IC 1613 (Hatt et al. 2017, hereafter Paper II). An overview of the observing program was presented by Beaton et al. (2016, hereafter Paper I). In addition, we have now begun an extension of the calibration of the TRGB to near-infrared

(*JHK*) wavelengths in two nearby galaxies, IC 1613 (Madore et al. 2018) and the Large Magellanic Cloud (LMC; Hoyt et al. 2018), which will provide added advantages for future studies from the ground and, especially, in space.

In this paper, we provide a summary of progress to date on the CCHP and apply the optical *I*-band TRGB calibration to the third release of SN Ia data from the Carnegie Supernova Project I (CSP-I). An overview of the CSP-I is given in Hamuy et al. (2006). The CSP-I has provided a well-observed, multiwavelength sample of SNe Ia recently published by Krisciunas et al. (2017). The outline of the paper is as follows. In Section 2 we discuss in more detail the motivation for the CCHP and describe the target galaxies and observations. In Section 3 we review the TRGB method, its calibration, and its application to our targets; we then provide a summary of the uncertainties in the method. In Section 4 we compare the distances measured using the TRGB to those obtained for the same galaxies using Cepheids. In Section 5 we discuss the very nearby (out to distances of 30 Mpc) Hubble diagram for the TRGB and Cepheid galaxies. In Section 6 we discuss the two independent SN Ia samples used in this analysis and the calibration for the absolute magnitudes of SNe Ia. In Section 7 we present the TRGB calibration of H_0 and a comparison with the Cepheid determination. In Section 7.5 we place in context other recent H_0 determinations and their uncertainties. In Section 8 we discuss future prospects for measuring a local value of H_0 to higher precision and better accuracy. Finally, in Section 9 we present a summary and the implications of our program at this juncture.

2. The CCHP

2.1. Overview and Motivation

As noted previously, the current goal of the CCHP is to increase both the precision and the accuracy of the TRGB method in order to provide an independent calibration of SNe Ia. The steps to a measurement of the local expansion rate through a “distance ladder” are straightforward. Fortunately, in recent years, the “rungs” in the distance ladder have been both significantly strengthened and reduced in number. Currently, only three steps are required for an accurate calibration of the extragalactic distance scale and a determination of H_0 :

1. an absolute zero-point calibration using geometric techniques (using, for example, trigonometric parallaxes, masers, and/or detached eclipsing binaries (DEBs));
2. absolute distances to a sample of galaxies that are hosts to one or more SN Ia events, which are simultaneously close enough to have their distances measured (using either Cepheids or, in the case of this paper, TRGB stars); and
3. high-precision relative distances to a statistically significant sample of galaxies far enough into the Hubble flow so that their peculiar velocities are a small fraction of the cosmological recessional velocities (using SNe Ia).

The largest contributors to the systematic uncertainty in H_0 are the first two items in the above list: the accuracy of the calibration of the local distance scale (its zero-point) and the total number of calibrators available to tie into the more distant Hubble flow. Increasingly larger samples of SNe Ia in the Hubble flow have only a small impact on the total uncertainty in the measurement of H_0 . One of the biggest remaining

⁹ Efstathiou (2014) undertook a reanalysis of the Riess et al. (2011) data, finding somewhat lower values of $H_0 = 70.6 \pm 3.3$ and $72.5 \pm 2.5 \text{ km s}^{-1} \text{ Mpc}^{-1}$, depending on what local calibration he adopted.

¹⁰ In the Carnegie Hubble Program (CHP), Freedman et al. (2012) based their value of H_0 on the Cepheid distance scale.

challenges to the local measurement of H_0 is set by the small number of nearby galaxies that are both host to SNe Ia and within reach of *HST* for measuring Cepheid distances. To date, there are only 19 published Cepheid distances for nearby SNe Ia observed with modern, linear detectors (Riess et al. 2016), resulting from almost 40 yr of SN Ia searches.¹¹

Type Ia SNe are rare events: those in a host galaxy close enough for high-accuracy measurements of Cepheids with *HST* occur, on average, only once every ~ 2 yr. Building up a larger sample with Cepheids alone could take decades. Nor will the *James Webb Space Telescope (JWST)* help in this regard, since Cepheids are relatively blue stars, and *JWST* is diffraction-limited at $2\ \mu\text{m}$. Hence, an additional method for measuring distances with similar precision and high accuracy to a larger number of nearby galaxies is important for a robust measurement of H_0 ; the TRGB method offers this opportunity. These red stars are also excellent targets for *JWST*.

2.2. Target Galaxies and Description of Observations

The primary recent focus of the CCHP has been the measurement of the TRGB in the halos of nine galaxies hosting a total of 11 SNe Ia. Observations were taken as part of an *HST* Cycle 22 GO proposal (Proposal 13691; Freedman 2014). Our targeted galaxies range in distance from 7 Mpc (M101) to almost 20 Mpc (NGC 1316, a member of the Fornax cluster). Data were obtained using the *HST*/Advanced Camera for Surveys (ACS) and the F814W and F606W filters; total exposure times ranged from 2×1100 to 12×1200 s. The target fields were carefully selected to cover the halos of the galaxies where the effects of dust are minimal while simultaneously avoiding contamination by younger and brighter disk asymptotic giant branch (AGB) stars. A montage of the CCHP target halo fields is shown in Figure 1. Further details of the observations of the individual galaxies can be found in Papers III–VII. In Figure 2, we show a montage of the fields analyzed by Jang & Lee (2017a).

In Table 1, we list the galaxies and their morphological types, foreground *I*-band extinctions, distances (in kpc), SN Ia names, and references for the individual distance analyses. In addition to the 11 SN Ia calibrators in our sample, we have also reexamined TRGB fits to the archival data for the galaxies analyzed earlier by Jang & Lee (2017a), yielding an additional five galaxies and five SNe Ia. Finally, NGC 1404, a galaxy also in the Fornax cluster, was host to both SN 2007on and SN 2011iv. Since we have observations for two Fornax galaxies (NGC 1365 and NGC 1316), we adopt the average distance for these two objects and apply it to NGC 1404, allowing us to add two further SN Ia calibrators (SN 2007on and SN 2011iv), for a total sample of 18.

The observed scatter in the magnitude–redshift relation for SNe Ia, observed as part of the CSP-I, amounts to only ± 0.10 mag (Burns et al. 2018). If this intrinsic scatter applies to the calibrating SNe Ia as well, then for a sample of 18 calibrators, this single uncertainty contributes $(0.1/\sqrt{17}) = 0.024$ mag, or 1.1%, to the overall systematic error budget. However, as we shall see in Section 6.4, the measured dispersion in the absolute magnitudes for the calibrator galaxies is slightly larger than that for the distant sample, amounting to ± 0.12 mag. This larger scatter reflects the (expected) added

uncertainty due to the fact that these SNe Ia were observed with a variety of telescopes and instruments, not all of which were as well characterized as the CSP-I observations. Moreover, the observed scatter in the calibrators will also include the individual uncertainties in the distances to each of the host galaxies.

3. The TRGB Distance Scale

3.1. Description of the TRGB and Its Theoretical Basis

The TRGB marks the onset of core helium burning (the helium flash) for low-mass red giants (see Salaris & Cassisi 1997; Serenelli et al. 2017). This feature is observed as a clear discontinuity in the first-ascent RGB luminosity function. As such, the TRGB provides a simple, empirically based (e.g., Lee et al. 1993; Rizzi et al. 2007) feature for measuring distances to nearby galaxies. The TRGB stars are distinctively bright and red ($M_I = -4.0$ mag, $(V - I) \sim 1.6$ mag), making them easily identifiable and measurable in the uncrowded halos of all types of nearby galaxies. From an astrophysical perspective, the theory of giant branch stellar evolution is a mature and well-understood subject (e.g., Salaris & Cassisi 1997; Bildsten et al. 2012; Serenelli et al. 2017). The bolometric TRGB is predicted to be only a weak function of metallicity (for $Z < 0.04$) and an even weaker function of mass (for evolved stars with masses $M < 1.4 M_\odot$ and parent population ages > 4 Gyr).

All of these (empirical and theoretical) characteristics combine to make the TRGB a superb standard candle. To date, most of the TRGB distance determinations have been carried out using the *I* band (the F814W filter on *HST*), where the bolometric corrections flatten the *I*-band luminosity of the observed TRGB as a function of color/metallicity (Salaris & Cassisi 1998; Cassisi & Salaris 2013; Serenelli et al. 2017).

3.2. Advantages and Disadvantages of the TRGB Method

Below, we enumerate and describe in more detail the many important advantages that the TRGB method has for measuring distances.

1. Most importantly, RGB stars that are located in galaxy halos suffer little reddening/extinction by *in situ* dust.
2. Relative to stars located in the higher surface density disks of galaxies, halo TRGB stars are quite isolated. As a result, they are minimally affected by crowding/blending effects.
3. Halo populations do not contain a significant population of brighter, intermediate-aged AGB stars that can make an accurate measurement of the TRGB more difficult.
4. The *I*-band TRGB is minimally affected by metallicity. Moreover, the metallicity of a TRGB star manifests itself directly in the star’s color (Salaris & Cassisi 1998), and thus a spread in metallicity is readily identifiable by a widening of the RGB in color. This effect can be corrected for and has been calibrated empirically (Rizzi et al. 2007; Mager et al. 2008; Madore et al. 2009; Jang & Lee 2017b).
5. Because all galaxies contain an old, early generation of stars, the TRGB method can be applied to galaxies of all morphological types, as well as those of all inclinations. Cepheids, in contrast, occur only in late-type (star-forming) galaxies and are difficult to detect in highly inclined galaxies.

¹¹ At the time of the Cycle 22 proposal, when this study was begun, only nine Cepheid measurements to SNe Ia were published (Riess et al. 2011).

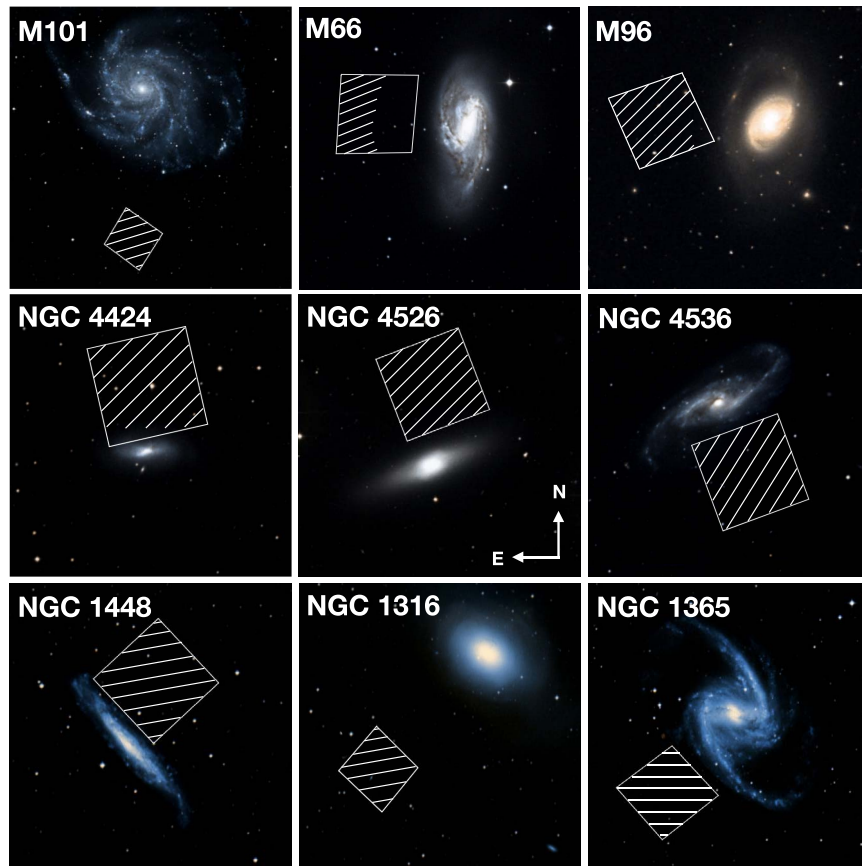


Figure 1. Images of the *HST/ACS* images for the nine TRGB galaxy fields observed as part of our program. The halo target fields in each case are outlined by boxes. The hatched regions indicate those analyzed in this study. North is up, and east is to the left.

6. Finally, from an observational perspective, the TRGB method offers a distinct advantage in observing efficiency. For Cepheids, at least a dozen observations, individually spread over a time baseline of several months, are needed to discover the variables, measure their light curves, and determine their periods, amplitudes, and mean magnitudes. Further observations sampling the light curves at one or more additional wavelengths are also needed to correct for reddening and constrain metallicity effects (Freedman et al. 2001; Riess et al. 2016). For the TRGB method, single-epoch exposures made in just two passbands are all that are required. The resulting color–magnitude diagram (using I versus $(V - I)$ or I versus $(I - J)$, say) allows the RGB population to be color-selected, and the TRGB magnitude is then distinguished by an abrupt discontinuity in the color-selected, marginalized I -band luminosity function.

A sometimes-cited disadvantage of the TRGB method with respect to Cepheids is that at optical wavelengths, TRGB stars are fainter than most of the Cepheids generally observed in external galaxies, typically those with periods greater than 10 days. However, because 12 phase points are needed to discover Cepheid variables, the total observing time required is actually comparable for both methods.¹² Moreover, the TRGB/Cepheid luminosity ratio reverses at near-infrared wavelengths, where TRGB star luminosities exceed those of 10 day Cepheids.

Ironically, for Cepheids in the H band, one of the primary contaminants of these variable stars are these same bright red giant (TRGB) stars that are both projected onto and located within the disk.

A cautionary flag for the application of the TRGB method is worth emphasizing: it should not be applied in high-surface-brightness regions (e.g., the inner disks or arms of spiral galaxies). Measurement of the TRGB must be focused on the halos of these galaxies; otherwise, disk AGB stars will contaminate the sample and could lead to spurious detections (e.g., Saviane et al. 2004, 2008), as later pointed out by Schweizer et al. (2008) and independently confirmed by Jang & Lee (2015) in the case of the Antennae galaxies, NGC 4038/39. Further examples of spurious detections are those of Maffei 1 and 2 (Wu et al. 2014; Tikhonov & Galazutdinova 2018; Anand et al. 2019). However, care must still be taken to sufficiently populate the TRGB so that small number statistics are not an issue (see, for example, Madore & Freedman 1995; Mager et al. 2008; Hatt et al. 2017). Attention to the selection of appropriate halo TRGB fields is straightforward, however, and these potential problems can be anticipated and largely avoided.

3.3. Measuring the TRGB

The use of RGB stars for measuring distances to nearby objects has had a long history, although only in recent decades has its full potential and utility been demonstrated. Originally Shapley (1918) used bright giants in the color–magnitude diagrams of globular clusters as one means to gauge the size of

¹² This is what allowed Jang & Lee (2017a) to measure the TRGB in distant galaxies targeted by *SHoES* by stacking the individual Cepheid frames.

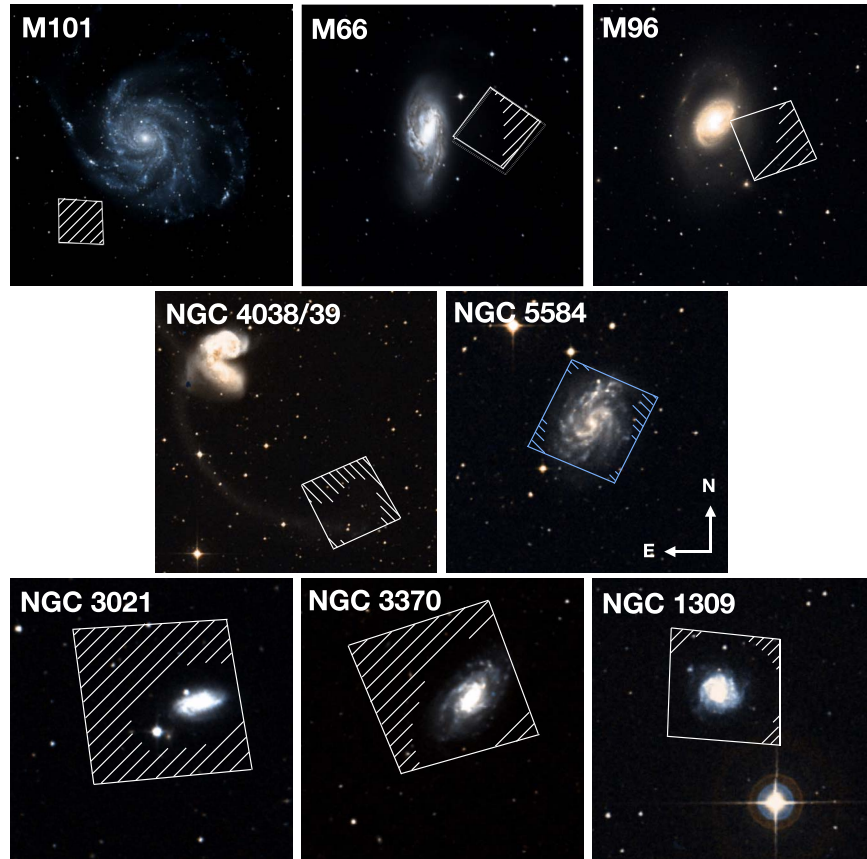


Figure 2. Images of the *HST* images for the eight TRGB galaxy fields analyzed by Jang & Lee (2017a). Here NGC 5584 was observed with WFC3; the remaining seven galaxies were observed with ACS. The Jang & Lee halo target fields in each case are outlined by boxes. The upper three images for M101, M66, and M96 are shown for comparison only; distances to the galaxies have been independently measured as part of the CCHP for the fields illustrated in Figure 1. The hatched regions indicate those analyzed by Jang & Lee (2017a). North is up, and east is to the left.

Table 1
TRGB Calibration Sample

Galaxy	Type ^a	A_I	d (kpc)	SN Name	Distance Reference
CCHP Program Galaxies					
M101 ^b	SAB(rs)cd	0.013	6.5	SN 2011fe	Beaton et al. (2019); Paper VII
M66 = NGC 3627 ^b	SAB(S)b	0.050	11.1	SN 1989B	Hoyt et al. (2019); Paper VI
M96 = NGC 3368 ^b	SAB(rs)ab	0.038	11.6	SN 1998bu	Hoyt et al. (2019); Paper VI
NGC 4536	SAB(rs)bc	0.027	15.6	SN 1981B	Hatt et al. (2018a); Paper IV
NGC 4526	SAB0(s), edge-on	0.033	15.8	SN 1994D	Hatt et al. (2018a); Paper IV
NGC 4424	SAB(s)	0.031	15.8	SN 2012cg	Hatt et al. (2018a); Paper IV
NGC 1448	SAcd, edge-on	0.021	18.4	SN 2001el	Hatt et al. (2018b); Paper V
NGC 1365	SB(s)b	0.031	18.7	SN 2012fr	Jang et al. (2018); Paper III
NGC 1316	SAB(0)peculiar	0.031	19.6	SN 1980N, 1981D, 2006dd	Hatt et al. (2018b); Paper V
NGC 1404	E1	0.017	19.3	SN 2007on, 2011iv	This paper
Our Adopted Distances for the Jang & Lee Galaxies					
M101 ^b	SAB(rs)cd	0.013	6.5	SN 2011fe	Jang & Lee (2017a)
M66 ^b	SAB(S)b	0.050	11.1	SN 1989B	Jang & Lee (2017a)
M96 ^b	SAB(rs)ab	0.038	11.6	SN 1998bu	Jang & Lee (2017a)
NGC 4038	SB(s)m pec	0.070	21.7	SN 2007 sr	Jang & Lee (2017a)
NGC 5584	SAB(rs)cd	0.059	23.1	SN 2007af	Jang & Lee (2017a)
NGC 3021	SA(rs)bc	0.020	27.8	SN 1995al	Jang & Lee (2017a)
NGC 3370	SA(s)c	0.046	28.5	SN 1994ae	Jang & Lee (2017a)
NGC 1309	SA(s)bc	0.060	31.6	SN 2002fk	Jang & Lee (2017a)

Notes.

^a From NED.

^b New (halo) fields in M101, M66, and M96 were observed as part of the CCHP. Archival fields for these galaxies were analyzed by Jang & Lee (2017a). We adopt the new CCHP distances for these galaxies presented in this paper.

the Milky Way; resolution of the brightest giants in M31, M32, and other Local Group galaxies led Baade (1944) to his recognition of two population types. Other historical examples can be found in the review by Madore & Freedman (1999, and references therein). In a more modern context, Mould & Kristian (1986) and Freedman (1988) obtained some of the first CCD observations of extragalactic stellar populations and used TRGB stars to measure the distances to several Local Group galaxies. Formalizing the technique further, Lee et al. (1993) introduced a quantitative edge detector for measuring the TRGB, convolving the luminosity function of the giant branch with a Sobel filter of the form $[-2, 0, +2]$. A Sobel (or gradient) filter determines a discrete first derivative; i.e., it is specifically designed for locating edges or sharp discontinuities. It is widely used for this purpose in image processing and analysis applications (e.g., Russ 1992).

A number of refinements to the basic technique have continued to be explored and applied over the past few decades (e.g., Madore & Freedman 1995; Sakai et al. 1996; Cioni et al. 2000; Méndez et al. 2002; Karachentsev et al. 2003, 2018; Mager et al. 2008). Recently, Hatt et al. (2017) and Jang et al. (2018) compared results for six different published variations of the basic edge detector for IC 1613 and NGC 1365, respectively. In the case of the nearby galaxy IC 1613, all six methods yielded agreement in the final distance modulus for the galaxy at the ~ 0.01 mag level, including our adopted method described below. In the case of NGC 1365, Jang et al. (2018) found a measured dispersion of about ± 0.04 mag, with some outliers. The method that we have adopted has been explicitly designed to minimize the uncertainties in the application of the edge detector encountered previously.

As described in detail in Hatt et al. (2017) and applied in Papers III–VII, our adopted procedure is to first smooth the observed giant branch luminosity function using a nonparametric interpolation technique: Gaussian-windowed, Locally Weighted Scatterplot Smoothing (GLOESS). We introduced GLOESS smoothing in this context because it is effective at suppressing false (noise-induced) edges, especially in the case of sparsely sampled bins in the luminosity function. It is a technique we have previously used for fitting variable-star light curves (see Persson et al. 2004; Monson et al. 2012, 2017). After smoothing, we then apply a simple $[-1, 0, +1]$ Sobel edge-detection kernel for the measurement of the TRGB.

For the analysis in this current paper, in order to ensure consistency across all of the galaxies in the program, we have re-reduced all of the SN Ia host galaxies in the CCHP program with DAOPHOT/ALLFRAME (Stetson 1987, 1994) using a single automated pipeline as described in Beaton et al. (2019). We have constructed a grid of synthetic point-spread functions (PSFs) from TinyTim (Krist et al. 2011) and use the same PSF for all of the frames of a given filter for all of the galaxies in the CCHP program. We have used a set of uniform criteria to define our photometry catalogs across the sample of galaxies, and in some cases, we have applied more stringent spatial cuts to avoid contamination by younger AGB stars. In Figure 3, we show the updated color-magnitude diagrams, luminosity functions, and Sobel filter output for our nine CCHP targets used for the analysis in this paper. The edge detection for all of the galaxies was also carried out independently by several of us, and the results were only cross-compared in the final stages of analysis. Next, the GLOESS smoothing was applied in a second pass, stepping iteratively through a range of smoothing

scales, to ensure that the peak in the luminosity function was not overbroadened. In order to suppress the effects of statistical noise fluctuations in any sparsely sampled bins in the luminosity function, we weighted the Sobel filter response inversely by the Poisson noise calculated in the adjacent bins in the smoothed luminosity function, as described in Hatt et al. (2017). The F814W TRGB magnitudes generally agree to within ± 0.04 mag with the values in Papers III–VII. This agreement is reassuring, given that these independent analyses utilize different methods for calculating aperture corrections, different smoothing scales were used for determining the TRGB magnitudes, and they were carried out by different individuals in separate analyses intended to allow us to provide external estimates of the uncertainties. Overall, our approach is both conceptually simple and, as verified by extensive artificial stars tests (Hatt et al. 2017; Jang et al. 2018; B. F. Madore & W. L. Freedman 2019, in preparation), it is also robust and provides quantifiable uncertainties.

3.4. Adopted Zero-point Calibration for the I-band TRGB

Our ultimate goal for the absolute calibration of the TRGB is that of geometric parallax measurements for Milky Way RGB stars being obtained by *Gaia*.¹³ *Gaia* is a European Space Agency satellite that is measuring parallaxes, proper motions, broadband photometry, and spectroscopy for over 1 billion stars in the Milky Way to unprecedented precision. In anticipation of *Gaia*, we have been using the robotic Three Hundred MilliMeter Telescope at Las Campanas (Monson et al. 2017) to obtain accurate *BVI* photometry for about 2000 RGB stars in the Milky Way. As discussed in Beaton et al. (2016), the projected *Gaia* parallax measurement for these bright giants is expected to ultimately provide a calibration of the TRGB to 0.5%.

In the *Gaia* second data release (DR2) of 2018 April, a significant zero-point offset of $\sim 30 \mu\text{as}$ was found with respect to the International Celestial Reference System defined by over 500,000 background quasars (Arenou et al. 2018; Lindegren et al. 2018). Given the improvement that will come in future *Gaia* data releases in 2020 and beyond,¹⁴ we have opted in the meantime to anchor our current zero-point using geometric distances to the LMC, as described below. We note that the zero-point of the TRGB distance scale remains one of the largest systematic uncertainties in our measurement of H_0 . Fortunately, significant further improvement in the *Gaia* parallaxes will be forthcoming within the next few years.

While awaiting improved parallax results from *Gaia*, we have updated the absolute magnitude calibration of the *I*-band TRGB for the LMC. This calibration has four components: (1) the (geometric) distance to the LMC, (2) measurement of the *I*-band TRGB in the LMC, (3) correction for the *I*-band extinction to the LMC TRGB stars, and (4) transformation from the ground-based Vega system to the *HST/ACS* Vega photometric system.

1. The LMC has two recently determined independent distance moduli, one having a partially based geometric calibration and the other that is directly geometric. Scowcroft et al. (2011) and Monson et al. (2012) used the *Spitzer Space Telescope* to measure mid-infrared

¹³ <https://www.cosmos.esa.int/web/gaia>

¹⁴ See www.cosmos.esa.int/web/gaia/release

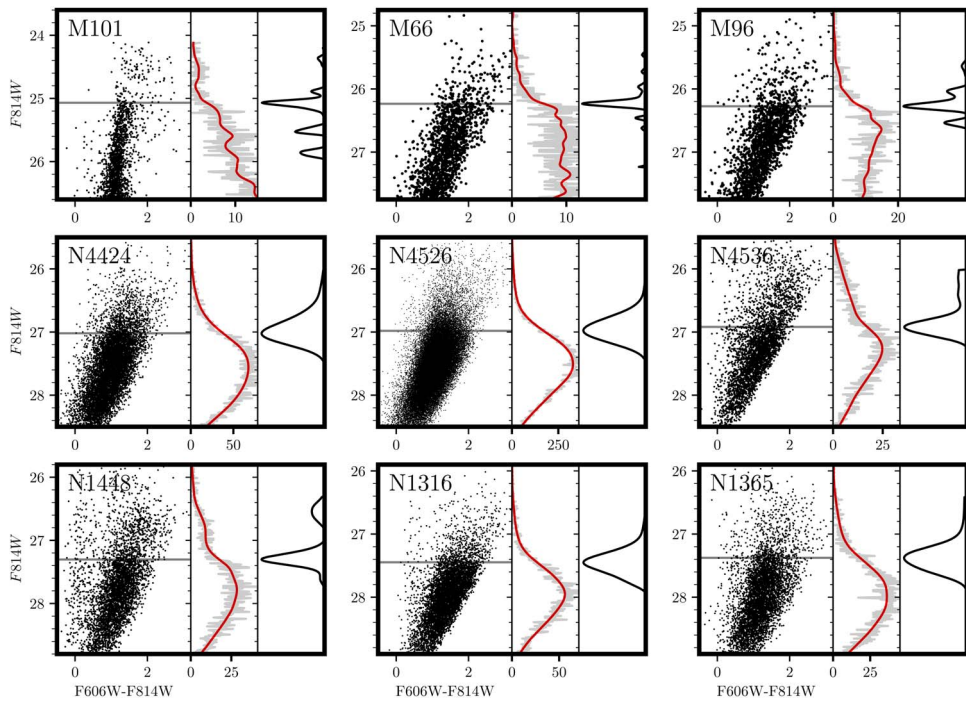


Figure 3. Color–magnitude diagrams (left panels), GLOESS-smoothed luminosity functions (red lines; middle panels), and the edge-detection response or Sobel filter output (right panels) for each of the nine CCHP galaxies. All of the data have been reduced using the same quality cuts based on DAOPHOT sharp and CHI values (Stetson 1994) using the automated pipeline developed for the CCHP (as described in Beaton et al. 2019). The position of the TRGB is indicated by the black horizontal lines in the color–magnitude diagrams, corresponding to the edge-detection response at right.

3.6 μm period–luminosity relations (the Leavitt law) for 10 Milky Way Cepheids with *HST* parallaxes (Benedict et al. 2007) and a sample of 85 Cepheids in the LMC. Based on these data, Freedman et al. (2012) found a resulting true LMC distance modulus of $\mu_o = 18.477 \pm 0.033$ mag (sys). A more recent determination that is based on measurements of 20 DEB stars in the LMC by Pietrzyński (2019) gives $\mu_{\text{LMC}} = 18.477 \pm 0.004$ (stat) ± 0.026 (sys), corresponding to a distance uncertainty of only 1.2%. The DEB value is identical to the Freedman et al. (2012) modulus, but it has a smaller systematic uncertainty. Combining these two (independent) measurements gives our finally adopted true distance modulus to the LMC of $\mu_o = 18.477 \pm 0.004$ (stat) ± 0.020 mag (sys) [$\pm 1.0\%$].

2. We have measured the I -band magnitude of the LMC TRGB using the OGLE-III catalog of Ulaczyk et al. (2012). A Sobel response-function fit to the OGLE-III I -band data, excluding an ellipse centered on the bar of the LMC (defined by $a = 6^{\circ}12$, $b = 1^{\circ}22$; LMC Center, 05 23 34.6–69 45 22; rotation angle = 6°), results in a tip detection at $I = 14.595 \pm 0.021$ (stat) ± 0.01 (sys) mag. Including the entire sample yields exact agreement, indicating that crowding/blending effects are not affecting the result. We show the color–magnitude diagram, luminosity function, and Sobel edge-detection filter output in Figure 4.
3. Recently, B. F. Madore & W. L. Freedman (2019, in preparation) made a direct measurement of the reddening for TRGB stars in the LMC. A brief summary of these results is given in Appendix A. The method is similar to that developed for Cepheid variables (e.g., Freedman 1988; Freedman et al. 2001; Riess et al. 2016). A comparison of multiwavelength ($VJHK$) magnitudes for TRGB stars in

the LMC can be made relative to similar multiwavelength observations of TRGB stars in other galaxies and provides a means to measure the differential extinction for the TRGB stars directly. We have compared the multiwavelength magnitudes for TRGB stars in the LMC (VI OGLE-III data from Ulaczyk et al. 2012 and JHK cross-matched 2MASS data from Zaritsky et al. 2004) with those in the SMC (Zaritsky et al. 2002) and IC 1613 (Hatt et al. 2017). Correcting these differential measurements for the small, independently measured SMC and IC 1613 reddenings then yields the total average reddening to the LMC TRGB stars. Multiwavelength differential distance moduli plots for the SMC and IC 1613 can be found in Appendix A. Fits to the multiwavelength differential moduli result in a determination of the LMC reddening of $E(B - V) = 0.093 \pm 0.01$ mag based on the SMC comparison and $E(B - V) = 0.096 \pm 0.01$ mag based on the IC 1613 comparison. These values are higher than our previously adopted value of $E(B - V) = 0.03 \pm 0.03$ mag (Hatt et al. 2018a, 2018b; Hoyt et al. 2018); however, the current measurement applies directly to the TRGB stars themselves. The corresponding extinctions in the I band are $A_I = 0.158 \pm 0.01$ and 0.162 ± 0.01 mag, respectively. Although formally, the error is 0.01 mag, we conservatively adopt a mean value of $A_I = 0.160 \pm 0.02$ mag.¹⁵ Our mean value of $A_I = 0.160$ mag (corresponding to $E(V - I) = 0.131$ mag) agrees to within the 1σ uncertainties (of ± 0.02 mag) with other recent reddening estimates of the LMC, based on a number of different methods (e.g., Joshi & Panchal 2019). We note that Haschke et al. (2011) found values of $E(V - I)$ of 0.11 and 0.09 for

¹⁵ We have also perturbed the solutions, allowing for a ± 0.03 mag uncertainty in the V and I zero-points. The average deviation in A_I is only 0.011 mag.

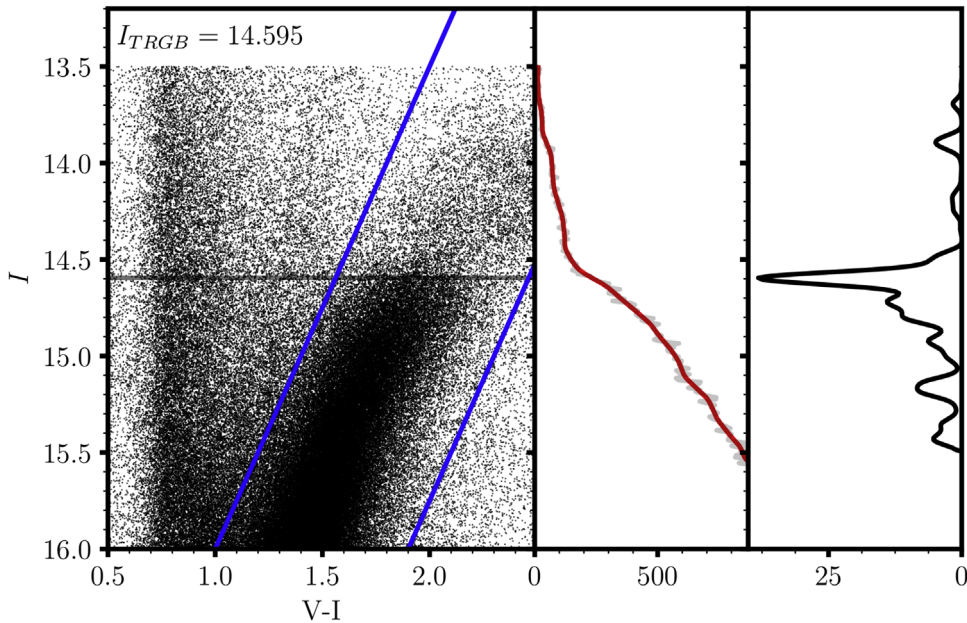


Figure 4. Color–magnitude diagram (left panel), GLOESS-smoothed luminosity function (red line; middle panel), and edge-detection response or Sobel filter output (right panel) for the outer region of the LMC (as defined in the text), based on the OGLE-III catalog from Ulaczyk et al. (2012).

LMC RR Lyrae and red clump stars, respectively, albeit with larger uncertainties of 0.07 and 0.06 mag.

- To transform from the ground-based I band (Vega system photometry) of Ulaczyk et al. (2012) into the Vega-based HST/ACS photometric system in F814W, we used the HST Wide Field Camera 3 (WFC3) calibration given by Riess et al. (2016). We note that the WFC3 F814W zero-point agrees to within -0.002 mag with that for ACS for F814W¹⁶:

$$m_{814W} = I + 0.02 - 0.018(V - I). \quad (1)$$

For a fiducial color of $(V - I) = 1.6$ mag for the LMC TRGB, this correction amounts to 0.0088 mag. Riess et al. (2016) concluded that the uncertainty in the zero-point of the transformation was <0.004 mag. We adopt this uncertainty as the statistical uncertainty alone. We compare this offset with that measured independently by Hatt et al. (2017) for ground-based photometry for standard stars in IC 1613 transformed to the ACS F814W photometric system, which provides an independent test of the zero-point. Hatt et al. (2017) found that $F814W = I - 0.02$ (their Figure 11), agreeing to within ± 0.01 mag with the value of 0.01 mag from Equation (1).¹⁷ Conservatively, we adopt an additional ± 0.02 mag systematic uncertainty for the I band-to-WFC3 transformation. We

¹⁶ <http://www.stsci.edu/hst/acs/documents/isrs/ir1710.pdf>

¹⁷ We note also that the recent recalibration by Riess et al. (2019), based on observations for LMC Cepheids, results in a difference (in the sense of ground- $HST/WFC3$) of 0.018 mag, with a standard deviation of 0.036 mag for the F814W observations. This offset would result in an absolute magnitude of $M_I^{\text{TRGB}} = -4.067$ mag (within our adopted uncertainty), which would lead to a 0.9% decrease in H_0 . At this time, we have not applied this (approximate) transformation, which, as Riess et al. (2019) noted, is for comparison purposes only. Finally, we note that this new calibration, applied to VH data for the Cepheids, has a larger impact on H_0 than in the case of the TRGB, resulting from the fact that for the Cepheids, the Wesenheit function, W , as defined by Riess et al. (2019), is $m_H^W = F160W - 0.386$ ($F555W$ – $F814W$). The offsets (ground- HST) for VH and m_H^W , after being transformed to on-flight magnitudes, amount to $+0.036$, $+0.018$, -0.032 , and -0.040 mag, respectively.

Table 2
Systematic Uncertainty in the TRGB Zero-point

Source	Value (mag)	σ_{stat}	σ_{sys}
$I_{\text{TRGB}}^{\text{LMC}}$	14.595	0.021	0.01
A_I^{LMC}	0.160	...	0.02
Metallicity	0.01
I band to WFC3	0.0088	0.004	0.02
WFC3 to ACS	-0.002	...	0.01
Adopted LMC true distance modulus	18.477	0.004	0.02
M_{814}^{TRGB}	-4.049	0.022	0.039

also include an additional ± 0.01 mag systematic uncertainty to account for the WFC3-to-ACS transformation and an additional ± 0.01 mag systematic uncertainty to account for metallicity.

Finally, A. G. Riess (2019, private communication) compared the OGLE-III I -band photometry with F814W ACS data for seven short-exposure fields in the LMC, allowing a comparison of RGB stars. He found a median difference of $\text{ACSF } 814W - I(\text{OGLE-III}) = 0.0035$ mag. This difference agrees well with the difference of $F814W - I$ based on the calibration adopted in Table 2, which amounts to $0.0088 - 0.002 = 0.0068$ mag; i.e., the difference is at the 0.0033 mag level. These various comparisons lend confidence that the current calibration of the LMC TRGB is accurate to within our quoted uncertainties.

When combined with our currently adopted LMC distance modulus of 18.477 ± 0.004 (stat) ± 0.020 (sys) mag and adding the uncertainties described above in quadrature, this yields $M_I = I_{\text{TRGB}}^{\text{LMC}} - \mu_{\text{LMC}} - A_I - zp = 14.595 - 18.477 - 0.160 - 0.0088 + 0.002 = -4.049$ mag ± 0.022 mag [1.0%] (stat) ± 0.039 mag [1.8%] (sys) for the I -band TRGB absolute zero-point calibration at the fiducial color of $(V - I) = 1.6$ mag. These sources of uncertainty are summarized in Table 2. Our adopted value of $M_I = -4.05$ mag is consistent with the range that has historically been published,

Table 3
TRGB Calibrator Distances

SN (1)	Galaxy (2)	μ_{TRGB} (3)	σ_T (4)	TRGB (5)	$m_{B'}$ ^{CSP} (6)	$\sigma_{B'}$ ^{CSP} (7)	$\mu_{\text{Ceph}}^{\text{a}}$ (8)	σ_C (9)	m_B^{SCb} (10)	σ_B^{SC} (11)	$V_{\text{NED}}^{\text{c}}$ (12)
1980N	N1316	31.46	0.04	CCHP	12.08	0.06	1306
1981B	N4536	30.96	0.05	CCHP	11.64	0.04	30.91	0.05	11.62	0.12	1050
1981D	N1316	31.46	0.04	CCHP	11.99	0.17	1306
1989B	N3627	30.22	0.04	CCHP	11.16	0.07	689
1990N	N4639	12.62	0.05	31.53	0.07	12.42	0.12	1050
1994D	N4526	31.00	0.07	CCHP	11.76	0.04	1050
1994ae	N3370	32.27	0.05	JL	12.94	0.05	32.07	0.05	12.92	0.12	1552
1995al	N3021	32.22	0.05	JL	13.02	0.05	32.50	0.09	12.97	0.12	1886
1998aq	N3982	12.46	0.05	31.74	0.07	12.24	0.12	1368
1998bu	N3368	30.31	0.04	CCHP	11.01	0.06	689
2001el	N1448	31.32	0.06	CCHP	12.30	0.04	31.31	0.04	12.20	0.12	1047
2002fk	N1309	32.50	0.07	JL	13.33	0.04	32.52	0.06	13.20	0.12	1864
2003du	U9391	13.47	0.09	32.92	0.06	13.47	0.11	2422
2005cf	N5917	12.96	0.07	32.26	0.1	13.01	0.12	2244
2006dd	N1316	31.46	0.04	CCHP	12.38	0.03	1306
2007af	N5584	31.82	0.1	JL	12.72	0.05	31.79	0.05	12.70	0.12	1983
2007ton	N1404	31.42	0.05	CCHP	12.39	0.07	1306
2007 sr	N4038	31.68	0.05	JL	12.30	0.15	31.29	0.11	12.24	0.11	1702
2009ig	N1015	13.29	0.05	32.50	0.08	13.46	0.12	2534
2011by	N3972	12.63	0.05	31.59	0.07	12.49	0.12	1368
2011fe	M101	29.08	0.04	CCHP	9.82	0.03	29.14	0.04	9.75	0.12	455
2011iv	N1404	31.42	0.05	CCHP	12.03	0.06	1306
2012cg	N4424	31.00	0.06	CCHP	11.72	0.06	31.08	0.29	11.55	0.11	1050
2012fr	N1365	31.36	0.05	CCHP	12.09	0.03	31.31	0.06	11.92	0.12	1302
2012ht	N3447	12.66	0.12	31.91	0.04	12.70	0.12	1447
2013dy	N7250	12.23	0.07	31.50	0.08	12.31	0.12	1410
2015F	N2442	12.40	0.03	31.51	0.05	12.28	0.14	1271

Notes.^a Cepheid distances from Table 5 of Riess et al. (2016).^b The SN peak B magnitudes. Riess et al. (2016) Table 5 gives $(m_B + 5a_B)$. Here $5a_B = 3.5635$ has been subtracted to give m_B . The definition of a_B is given in Equation (5) of Riess et al. (2016).^c Velocities listed here (in km s^{-1}) are computed from the galaxy redshifts using the linear multi-attractor model provided by NED. Some galaxies are also members of groups, and further details of their group membership and adopted velocities can be found in Appendix B.

$-4.00 \text{ mag} < M_I^{\text{TRGB}} < -4.05 \text{ mag}$ (e.g., Lee et al. 1993; Bellazzini et al. 2001; Rizzi et al. 2007; Jang & Lee 2017a), in addition to being consistent with recent *Gaia* DR2 parallax results for Milky Way TRGB stars given by Mould et al. (2019). We note that if we were to force our TRGB calibration to agree with the most recent value of $H_0 = 74.22 \text{ km s}^{-1} \text{ Mpc}^{-1}$ based on the LMC distance alone (Riess et al. 2019), that would imply a magnitude shift of 0.13 mag, or a value of $M_I^{\text{TRGB}} = -3.92 \text{ mag}$.

3.5. TRGB Calibrator Distances to SN Ia Host Galaxies

In Table 3, we list the SN and host-galaxy names, followed by the TRGB distance moduli and uncertainties, the apparent B' peak magnitudes and uncertainties for the CSP-I calibrators (see Section 6.2), the Cepheid distance moduli and uncertainties, the *SHoES* apparent B peak magnitudes and uncertainties (from Riess et al. 2016, their Table 5), and the velocity from the NASA Extragalactic Database (NED)¹⁸, corrected for the local flow for 27 nearby SNe Ia. The TRGB distance moduli for each of our

nine target galaxies were measured as described in Section 3.3 and calibrated by adoption of the zero-point given in Section 3.4. Also listed are the galaxies with distances measured and updated by Jang & Lee (2017a, their Table 3) and updated to our adopted TRGB zero-point. We have remeasured the TRGB using techniques as similar as possible to those used for the CCHP galaxies and found excellent agreement, with the exception of the galaxy NGC 5584. In this case, we have increased the distance modulus uncertainty to $\pm 0.1 \text{ mag}$ to reflect this difference. The Cepheid distances are taken directly from Table 5 of Riess et al. (2016), which is based on a calibration using Milky Way parallaxes, NGC 4258 masers, and LMC DEBs.

3.6. Summary of Uncertainties

Here we first provide a description of the known and potential sources of uncertainty (both statistical and systematic) that have gone into the adopted errors in the measurement of individual TRGB distances as given in columns 3 and 4 of Table 3. We then turn to a discussion of the overall systematic uncertainty for the ensemble sample of TRGB calibrators that is critical for our determination of H_0 (in Section 3.6.2).

3.6.1. Uncertainties for Individual TRGB Galaxy Distances

1. *Photometric errors and edge detection.* In the previous papers in this series (Papers III–VII), we have provided

¹⁸ We have compared our adopted velocities with the cosmicflows3 velocities (Graziani et al. 2019; http://www2.iap.fr/users/lavaux/science/2mrs_vel.html) and found, for the 24 galaxies in our sample, that the mean offset between CF-3 and NED (group membership-corrected) velocities is $28 \pm 150 \text{ km s}^{-1}$. However, the choice of velocities for these galaxies is not of importance in the context of measuring H_0 ; rather, the distances alone provide the calibration of H_0 .

detailed discussions and tabulations of the errors in the photometry for each of the galaxies in the CCHP sample. These include the photometric errors returned by DAOPHOT, aperture corrections from the PSF magnitudes to a 0''.5 aperture, and correction to infinite radius and transformation to the ACS Vega photometric system. In the case of the LMC, we have transformed our photometry from the ground-based Kron–Cousins I -band system to the ACS Vega system, as described in Section 3.4. The foreground galactic extinction corrections, applied on a galaxy-by-galaxy basis, have been adopted from Schlafly & Finkbeiner (2011), as tabulated in NED. For each of our program galaxies, we have undertaken extensive artificial star tests to quantify the effects of crowding and blending on our photometry, as well as to assess their effects on the edge detection and measurement of the TRGB. In some cases, we have opted to be more conservative with the error estimates listed in Table 3 than in the previously published papers. Overall, we impose a minimum error of ± 0.04 mag, despite the formal errors, in some cases, being as low as ± 0.02 mag.

2. *AGB contribution.* The known presence of oxygen-rich AGB stars in the 1 mag interval above and at about the same color as the TRGB acts as a source of elevated baseline noise in the application of edge-detection algorithms. This AGB presence lowers the contrast of the tip discontinuity, increasing the uncertainty in the measurement of the tip location. In practice, the effect of the AGB population on the TRGB is somewhat decreased by the fact that in high-precision data, a noticeable drop is seen in the AGB luminosity function in the 0.2 mag interval immediately above the TRGB. This has the effect of restoring some of the contrast of the TRGB tip discontinuity at the tip for high signal-to-noise data. We explicitly incorporate an AGB population into the derivation of an error budget for the tip detection. As described in detail in Hatt et al. (2017), Jang et al. (2018), Hatt et al. (2018a, 2018b), we have quantified this effect in our individual target galaxies using artificial star tests.

3. *Metallicity.* As discussed in Section 3.1, at optical (B and V) wavelengths, theory predicts and observations confirm that the reddest, high-metallicity stars will exhibit a downward slope of the TRGB in the color–magnitude diagram (e.g., Mager et al. 2008; Jang & Lee 2017a). However, the bolometric corrections work to flatten the tip in the observed redder I -band color–magnitude diagram. We have found that most of the metal-poor stars observed in our target galaxy halos show a negligible color–magnitude slope, necessitating no correction. At high metallicity, there is a (slight) slope to the I -band TRGB; however, in practice, since the most metal-poor stars are brighter than the metal-rich tip stars, the Sobel edge detector triggers a measurement of the edge discontinuity set by the bluer and brighter metal-poor stars. The redder (and more metal-rich) stars fall to lower luminosities and thereby no longer contribute to the detection of the edge in the luminosity function. We have experimented with correcting for the slope of the TRGB as in Mager et al. (2008) and find that the results do not differ significantly in precision or accuracy. We have included a metallicity uncertainty of ± 0.01 mag.

4. *Absolute zero-point.* In advance of obtaining a calibration from *Gaia* parallaxes applied to Milky Way field TRGB stars, we have established our zero-point using TRGB stars in the LMC. Following our discussion in Section 3.4, we adopt a systematic uncertainty of ± 0.039 mag (1.8%) for the overall zero-point for the I -band TRGB calibration.

In summary, σ_T , given for each galaxy in Table 3, is defined by $\sigma_T^2 = \sigma_{\text{phot}}^2 + \sigma_{\text{edge}}^2 + \sigma_Z^2$, where the photometric error is typically ± 0.03 mag, the edge-detection error is typically ± 0.03 mag, and the metallicity uncertainty is taken to be ± 0.01 mag, giving a baseline global statistical TRGB measurement uncertainty of ± 0.04 mag. The remaining uncertainties due to potential contamination by AGB stars are determined for each individual galaxy by the individual artificial star tests.

3.6.2. Overall Systematic Errors

Most of the sources of systematic uncertainty relevant to the determination of the error for an individual galaxy distance become random uncertainties when collectively applied to the determination of H_0 . For example, while an error in the individually measured aperture corrections will contribute a systematic uncertainty to the distance measurement of a given galaxy, for the ensemble of the calibrating sample, the aperture-correction uncertainties combine simply as random or statistical uncertainties. The individual distance uncertainties do, however, determine the weight that each galaxy distance carries in the calibration of the distant SNe Ia. On the other hand, three of the sources of uncertainty, those of the LMC ground-based I -band transformation to the *HST*/ACS F814W photometric system, the I -band extinction for the LMC TRGB stars, and the uncertainty on the LMC distance, carry over as systematic uncertainties on the zero-point calibration and determination of H_0 . We carry these three uncertainties forward in determining the overall systematic error in H_0 and distinguish them from the statistical uncertainties. We also allow for an overall systematic error due to metallicity. We return to a discussion of the systematic errors after application of the TRGB calibration to the distant SNe Ia in Section 7. The final uncertainty in H_0 combines, in quadrature, the systematic uncertainty given here with the uncertainty determined in our Markov chain Monte Carlo (MCMC) analysis of the SNe Ia alone, as discussed in Section 7.1.

The largest two contributing factors to the uncertainty in the local determination of H_0 are (1) the absolute zero-points of the Cepheid and/or TRGB distance scales (as described in Section 3.6.1, point 4) and (2) the numbers of Cepheid and/or TRGB calibrated galaxies hosting SNe Ia (Riess et al. 2016; Burns et al. 2018). Regarding the first, improvement of the calibration of the Cepheid and TRGB distance scales will come from future absolute trigonometric parallax measurements being carried out by *Gaia* (Lindegren et al. 2018); it is anticipated that direct geometric parallaxes will provide zero-points to better than 1% certainty for both the Cepheid and TRGB distance scales.

Our study is currently focused on decreasing the second source of systematic uncertainty by increasing the numbers of TRGB zero-point calibrators for measuring the absolute magnitudes of SNe Ia. The measured scatter in the B -band absolute magnitudes of the calibrating sample of CSP-I SNe Ia is ± 0.12 mag (see Section 6.4). With 18 TRGB

calibrators, a simple frequentist estimate of the uncertainty in the mean absolute magnitude for SNe Ia amounts to ± 0.029 mag (i.e., $0.12/\sqrt{17}$ mag), which will contribute a 1.3% uncertainty to the overall Hubble constant error budget. When the uncertainty in the zero-point of the TRGB is resolved by the expected *Gaia* release (in 2022), the dominant term in the Hubble constant error budget will become the number of TRGB distances calibrating the SN Ia zero-point.

An additional (but very small) uncertainty is contributed by the scatter in the far-field SN Ia sample. For a sample of 100 SNe Ia, this contributes $\pm 0.10/\sqrt{99} = \pm 0.01$ mag. In what follows, the errors for the CSP-I SNe Ia are calculated formally from the diagonal elements of the covariance matrix from our MCMC analysis (as discussed in Section 6.2).

4. TRGB and Cepheid Distance Comparison

A primary goal in the design of *HST* was to optimize the discovery and use of Cepheid variables in the calibration of H_0 , and it has proven to be highly effective for this purpose (Freedman et al. 2001; Sandage et al. 2006; Riess et al. 2016, and references therein). Indeed, for the past century, Cepheids have served as a “gold standard” for measuring the distances to nearby galaxies. The list of strengths for Cepheids in measuring extragalactic distances remains long (e.g., see the reviews by Madore & Freedman 1991; Freedman & Madore 2010) and includes the small observed dispersion in the Leavitt law, especially at longer wavelengths (e.g., see the first application by McGonegal et al. 1982); their clear signal through their distinctive variability and large amplitudes at short wavelengths; and the ability to correct for or minimize systematic effects due to reddening and metallicity using multiwavelength observations (see the first applications by Freedman et al. 1985; Freedman 1988; Freedman & Madore 1990). To date, the distances to 64 nearby spiral and irregular galaxies have been measured using Cepheids (NED: <https://ned.ipac.caltech.edu>; 2018 June 22 release). Hence, to be useful as an independent calibration of H_0 , any competing distance indicators must demonstrate that they are quantitatively at least as accurate as the Cepheids. Unfortunately, there are few methods available for which both the statistical and systematic uncertainties rival those of Cepheids. For example, there is only one galaxy, NGC 4258 at 7 Mpc, for which a maser distance has been measured and that can also be used as a zero-point calibrator (Herrnstein et al. 1999; Humphreys et al. 2013). Similarly, an accurate application of the DEB method has been confined to the nearby LMC (Pietrzynski et al. 2013; Pietrzynski 2019).

In the top panel of Figure 5, we show a comparison of published TRGB and Cepheid distance moduli for 28 galaxies. The distances are drawn from the compilations by Rizzi et al. (2007), Tully et al. (2013, 2015), Riess et al. 2016 (updated to the Cepheid recalibration of Riess et al. 2019), NED, and this paper. All of the TRGB distances have been recalibrated to our zero-point of $M_I^{\text{TRGB}} = -4.05$ mag. The galaxies span a range of a factor of 60 in distance (50 kpc–30 Mpc). As can be seen, the overall agreement between the two methods is very good. The rms dispersion about a slope-of-unity line is ± 0.11 mag. A residual difference plot is shown in the bottom panel (where $\Delta\mu = \mu_{\text{TRGB}} - \mu_{\text{Ceph}}$). The comparison illustrates the internal consistency of the nearby Cepheid and TRGB distance scales to a level of 5% in precision in the combined errors and reaffirms that the TRGB method is competitive with the Cepheid Leavitt law (see also earlier studies by Lee et al. 1993;

Ferrarese et al. 2000; Rizzi et al. 2007). Moreover, excluding the 10 distant galaxies that are hosts to SNe Ia (shown separately in Figure 6), the dispersion drops to only ± 0.05 mag, or 2% in distance. For the nearest galaxies, the methods show superb agreement.

In Figure 6, we show a comparison of TRGB and Cepheid distance moduli focusing on the 10 SN Ia host galaxies that have both TRGB and Cepheid distances, as presented in Table 3. Red filled circles represent the galaxies with TRGB distances measured as part of this study. These galaxies cover a range of distances from 7 Mpc (M101) to almost 20 Mpc (NGC 1316). Red open circles denote the galaxies analyzed by Jang & Lee (2017a). In this case, these galaxies extend out to distances beyond 30 Mpc. We compare to the LMC-only calibration for Cepheids from Riess et al. (2019). The rms scatter about the slope unity line illustrated is ± 0.17 mag. The difference ($\Delta\mu = \mu_{\text{TRGB}} - \mu_{\text{Ceph}}$) is plotted as a function of TRGB distance modulus in the bottom panel. The weighted average difference in distance modulus (TRGB minus Cepheid) amounts to $+0.059$ mag.

The scatter in the galaxy-to-galaxy comparison noted above for the TRGB and Cepheid distances amounts to ± 0.17 mag. Equally apportioning the resulting uncertainty between the two methods would correspond to an uncertainty of ± 0.12 mag for each method, or $\pm 6\%$ in distance. The scatter seen in Figure 6 is significantly larger than that for the more nearby galaxies shown in Figure 5, where the scatter amounts to only ± 0.05 mag, or $\pm 2\%$ in distance. The scatter in the Cepheid/TRGB overlap sample is also larger than indicated by the individually measured errors for the individual galaxies and suggests that the errors in the distances have been underestimated. The source of this additional uncertainty is unknown at present, and it is unclear whether both the TRGB and Cepheid distances share equally in the uncertainties. As we shall see in Section 5, the scatter in the local Hubble diagram is smaller by a factor of 1.4 for the TRGB calibrating galaxies than it is for the Cepheid calibrating galaxies, suggesting that the scatter in the comparison is not equally shared, but rather that the TRGB distances are more precise than the Cepheid distances.

5. The Nearby Hubble Diagram

In Figure 7, we plot a local Hubble diagram for very nearby galaxies, with TRGB (left panel) and (*SHoES*) Cepheid (right panel) distances to SN Ia host galaxies as a function of velocity. The galaxies for which both Cepheid and TRGB distances have been measured are shown as black filled circles in both plots. For nearby galaxies ($v \ll c$), the redshift provides a good approximation to the Hubble velocity, but the inhomogeneous distribution of matter in the universe results in deviations from the Hubble expansion. These induced “peculiar velocities” can be a significant component on top of the Hubble recessional velocity at low redshift. We have corrected the observed redshifts on a galaxy-by-galaxy basis using the linear multi-attractor model provided by NED. This model is defined by Virgo infall, the Great Attractor, and the Shapley supercluster (Mould et al. 2000). The adopted velocities are given in Table 3, and more detailed notes on individual galaxies and group membership, if applicable, can be found in Appendix B. A line with a slope of $H_0 = 70 \text{ km s}^{-1} \text{ Mpc}^{-1}$ and an intercept of zero is shown for reference.

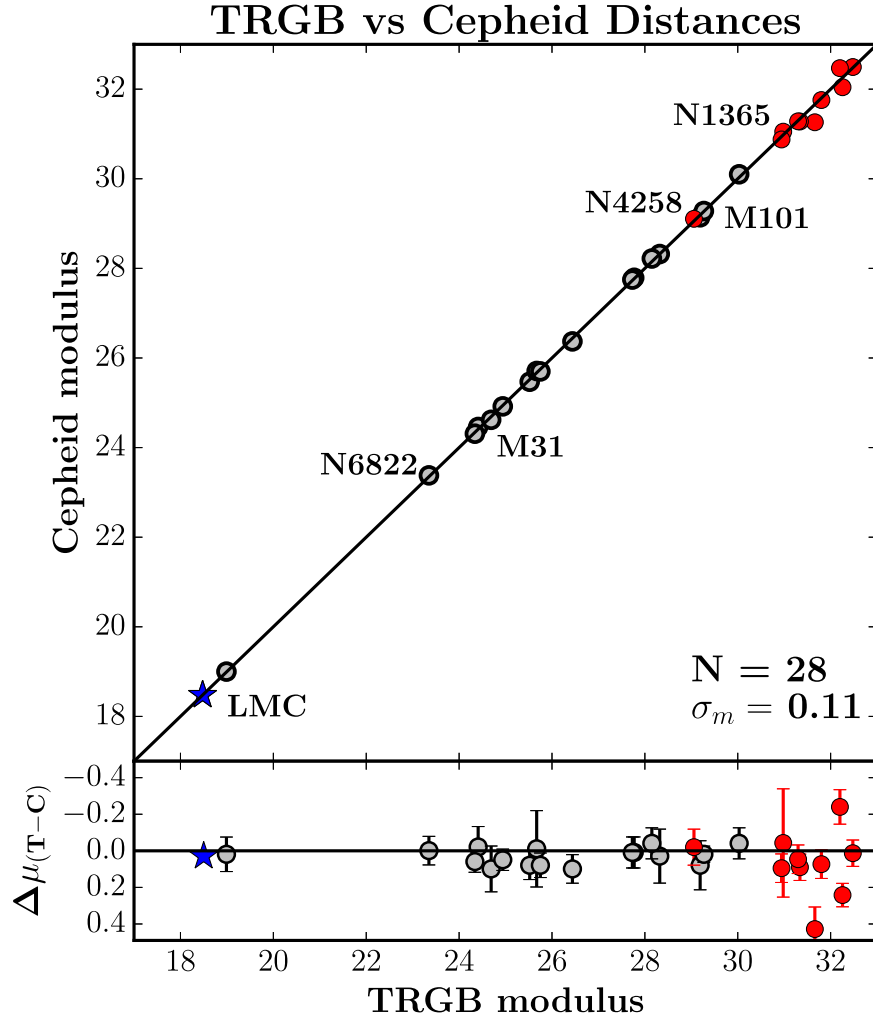


Figure 5. Top panel: comparison of published TRGB and Cepheid distance moduli for 28 nearby galaxies. The distances span a range from 50 kpc to 30 Mpc. The points in red are the calibrating galaxies that are host to SNe Ia, used in this study. Gray circled points are from the literature. The LMC, which provides the TRGB zero-point calibration, is shown as a blue star. The black line has a unit slope, and the dispersion about the line is ± 0.11 mag. Bottom panel: difference (TRGB minus Cepheid distance modulus) as a function of the TRGB modulus.

For the overlap sample of 10 galaxies that have both TRGB and Cepheid distances measured, we note that the ratio of the dispersion about independent fits to the TRGB and Cepheid data is 0.7. Since the galaxy velocity is the same in each individual case, this indicates that the uncertainty in the distances for the TRGB method is about a factor of 1.4 smaller than that for the Cepheids. A more detailed intercomparison and decomposition of the magnitude and origin of the scatter in the two panels of Figure 7 leads to a very similar conclusion. We fix the quadrature-summed dispersion σ_{TC} shared by the two distance indicators, where σ_C is the intrinsic Cepheid dispersion and σ_T is the intrinsic TRGB dispersion. Then, $\sigma_{TC} = (\sigma_C^2 + \sigma_T^2)^{1/2} = 0.17$ mag. Incrementally adding a peculiar motion component σ_{pec} simultaneously to each of the two velocity-distance plots, we find a best-fit solution to the data in the two diagrams with $\sigma_{\text{pec}} = \pm 130 \text{ km s}^{-1}$, $\sigma_C = \pm 0.14$ mag, and $\sigma_T = \pm 0.10$ mag, again confirming the higher precision of the TRGB distances in comparison to the Cepheid-based distances.

We note here that the Cepheid-based calibration of H_0 involves greater complexity in its application relative to that of the TRGB. For instance, Cepheids possess a range of periods; exhibit a width to the Leavitt law, which is a function of the

intrinsic temperature of the star; and suffer larger total and differential reddening. In addition, the effect of metallicity on the luminosities and colors of Cepheids as a function of wavelength still remains under discussion. Currently, Cepheids beyond the LMC are too faint to have their metallicities measured directly, requiring the use of a proxy metallicity indicator derived from young H II regions. Some studies have indicated that there may be a break in the slope of the Leavitt law at a period of 10 days (e.g., see discussions in Ngeow & Kanbur 2005; Ngeow et al. 2005; Riess et al. 2016). Possibly the most significant challenge for Cepheid measurements beyond 20 Mpc is crowding and blending from redder (RGB and AGB) disk stars, particularly for near-infrared H -band measurements of Cepheids. While a global fit can be applied to the entire Cepheid sample when marginalizing over these and other nuisance parameters, we note that these issues do not apply to the single-step measurement technique used for TRGB distances.

6. SNe Ia

Although the details of what gives rise to SN Ia explosions are not well understood from theory, the observed properties of

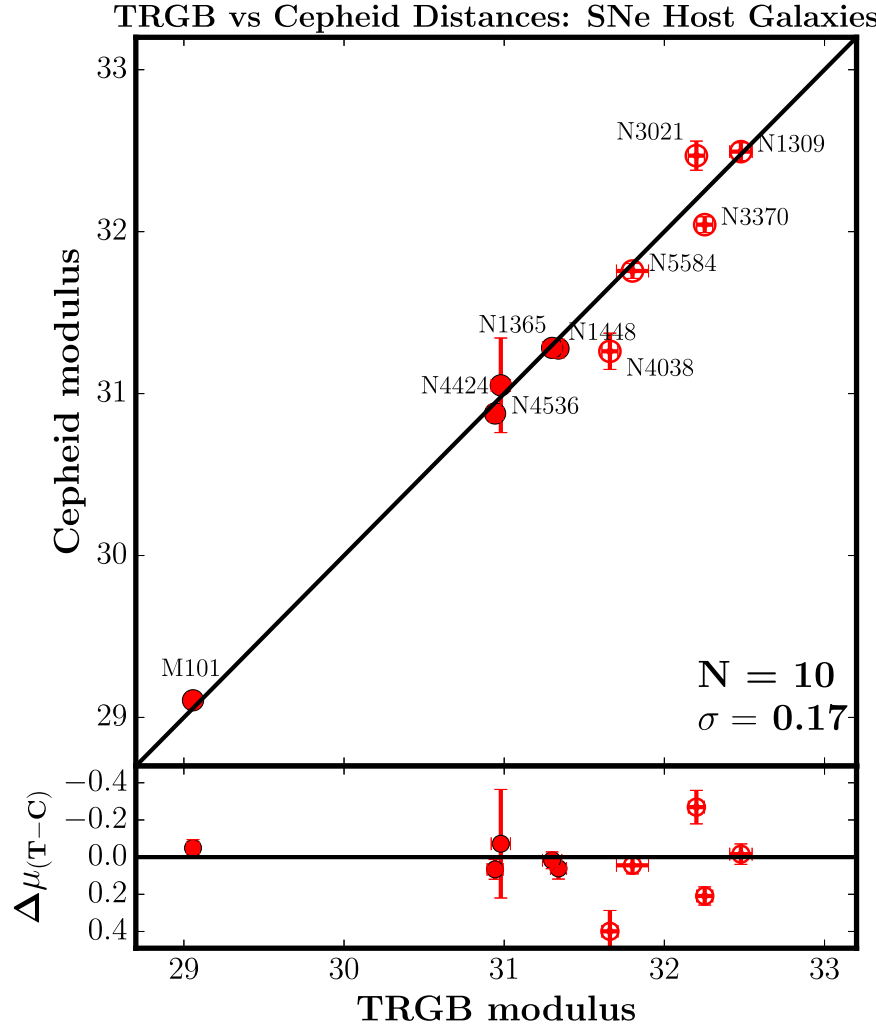


Figure 6. Top panel: expanded comparison of TRGB and Cepheid distance moduli for the subset of 10 nearby galaxies that also host SNe Ia. The distances span a range from 7 to over 30 Mpc. Red filled circles are galaxies with distances measured as part of the CCHP. Red open circles are those measured in the study of Jang & Lee (2017a). The black line has a unit slope, and the dispersion about the line is ± 0.17 mag. Bottom panel: difference (TRGB minus Cepheid distance modulus) as a function of the TRGB modulus. The weighted average difference in distance modulus (TRGB minus Cepheid) amounts to $+0.059$ mag.

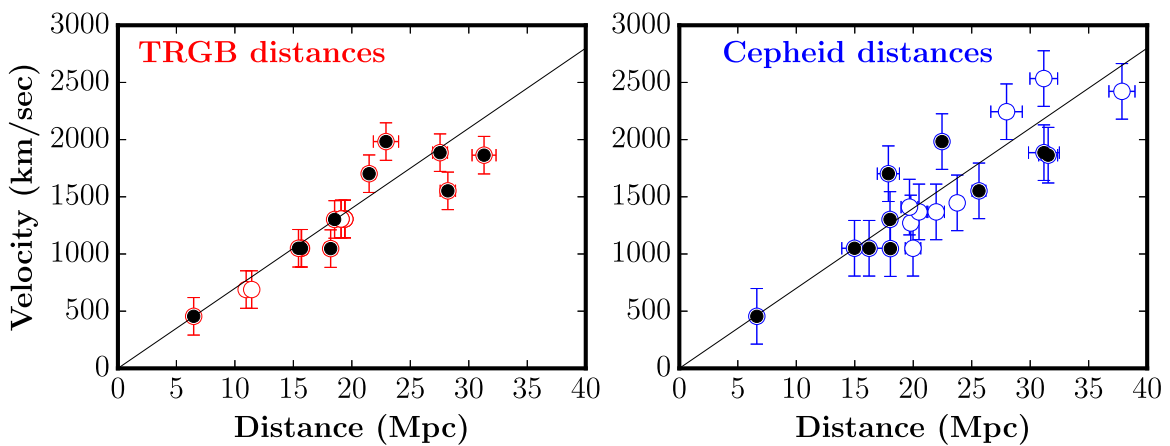


Figure 7. Nearby Hubble diagram for galaxies with TRGB (left panel) and Cepheid (right panel) distances. The black filled circles are for galaxies in common with both the TRGB and Cepheid samples. As described in the text, the velocities to these objects have been corrected for the presence of nearby mass concentrations using NED, as described in Section 5 and Appendix B. A slope of $H_0 = 70 \text{ km s}^{-1} \text{ Mpc}^{-1}$ is shown in black.

SNe Ia have, for many decades, been consistent with a general model in which an increase in the mass of a carbon–oxygen white dwarf in a binary system results in it approaching its Chandrasekhar mass ($1.4 M_\odot$), thereby triggering a

thermonuclear explosion (Hoyle & Fowler 1960; Wheeler & Hansen 1971). These events are predicted to occur if the white dwarf accretes material from a nearby companion star or, alternatively, if the companion itself is also a white dwarf, and

the merger of the two white dwarfs then triggers the explosion. Current observations seem to suggest that both single- and double-degenerate types of events may occur (e.g., see the recent review by Livio & Mazzali 2018).

Type Ia SNe have many observational advantages for determining the far-field value of H_0 (as well as other cosmological parameters), and as a result, they continue to play a pivotal role in cosmology. Primarily due to their high intrinsic luminosities, they can be observed well into the Hubble flow, where peculiar motions become a negligible contribution to their observed redshifts. In addition, because SNe Ia are transients and fade with time, image differencing (once the SN Ia has faded) permits very clean estimates of the flux, minimally affected by crowding issues. Brighter SNe Ia have wider light curves (longer decay times) than their fainter counterparts; correction for this simple empirical fact allows these objects to be used as standardizable candles (Phillips 1993; Riess et al. 1998; Perlmutter et al. 1999; Burns et al. 2018). As noted previously, for nearby, well-observed SNe Ia, their measured dispersion amounts to only ± 0.10 mag, or 5% in distance (Burns et al. 2018), depending on the filter/color combination employed. To date, no other method can provide relative distances to this precision in the redshift range $0.03 < z < 0.4$. However, SNe Ia are sufficiently rare and distant that determination of absolute distances requires an intermediate calibration step.

In what follows, we apply our new TRGB distances to the calibration of two published sets of SN Ia photometry: the CSP-I sample (Krisciunas et al. 2017) and the Supercal sample (Scolnic et al. 2015). We also compare the TRGB calibration to that based on the Cepheid data from Riess et al. (2016), as recalibrated by Riess et al. (2019). First, however, we turn our attention to potential systematic uncertainties affecting the peak luminosities of SNe Ia.

6.1. Systematic Uncertainties

Uncertainty remains as to whether there may be systematic effects in different SN Ia samples arising from different properties of the SN Ia progenitors located in different environments. For instance, an empirically well-established correlation has been measured (by many different groups) between the standardized peak luminosity of the SN Ia (after correcting for light-curve shape and color) and the total stellar mass of the host galaxy (Kelly et al. 2010; Lampeitl et al. 2010; Sullivan et al. 2010; Chidress et al. 2013; Uddin et al. 2017). The sense of the correlation is that, on average, SNe Ia residing in more massive galaxies are more luminous (although the mass of the host galaxy is unlikely to be the actual driver of the SN Ia luminosity difference). Furthermore, other groups have found correlations between the standardized peak luminosity and host-galaxy specific star formation rates, age, metallicity, and morphology (e.g., see Rigault et al. 2015, and references therein), many of which are covariant with host-galaxy mass.

This broad issue of environment is of importance in the context of the measurement of an accurate value of H_0 : if, for instance, the properties of the local calibrating sample of galaxies differ from those of the distant sample, it could potentially introduce a systematic error in H_0 . Cepheid variables are young objects found only in star-forming spiral galaxies and cannot calibrate SNe Ia found in elliptical or S \otimes galaxies. The distant samples of SNe Ia, however, are found in

galaxies with a much wider range of morphologies. These include late- and early-type spirals, gas-poor lenticular and elliptical galaxies having a range of masses, ages, star formation rates, and metallicities. An advantage of TRGB stars is that they are found in galaxies of all morphological types. We undertake our analysis of the TRGB calibration for the CSP-I both with and without a correction for host-galaxy mass, analogous to the Cepheid calibration carried out by Burns et al. (2018).

6.2. The CSP-I

Our primary sample of SNe Ia for this study comes from the CSP-I (Krisciunas et al. 2017).¹⁹ The CSP-I observations were obtained at Las Campanas Observatory over a 5 yr period, 2004–2009. The light curves for these SNe Ia are well sampled at $uBVgriYJH$, with most of the objects observed well before maximum. These data form the most homogeneous and densely sampled multiwavelength set of photometry measured for SNe Ia to date. The high quality of the photometry (Krisciunas et al. 2017) and the consistency of instruments/calibration/procedures used in the data reduction minimizes systematic differences that can be a challenge in combining multiple data sets and makes this an ideal sample for cosmological studies. An extensive set of optical spectra were also obtained as part of the CSP-I (Folatelli et al. 2013). The sample covers a range in redshift from 0.004 to 0.083 (1200–25,000 km s $^{-1}$). The data presented in Krisciunas et al. (2017) provide a synthesis of the previous publications in the CSP-I series and supersede those studies.

Details of the light-curve fitting for the CSP-I data using the SNoPy package can be found in Burns et al. (2018) and references therein. SNoPy utilizes a color-stretch parameter (s_{BV}) that proves to be very effective for also fitting fast-declining SNe Ia, which have often been excluded in other studies. This is advantageous for our determination of H_0 , since two of our calibrators (SN 2007on and SN 2011iv, in NGC 1404) are transitional between the fast decliners and normal SNe Ia. In Table 4, we provide literature references to the optical and near-infrared SN Ia photometry for the TRGB and Cepheid calibrator galaxies. Fits to the CSP-I data, in machine-readable form, were published by Burns et al. (2018).

In this paper, we analyze a subset of 104 (out of the total sample of 123) well-observed, high signal-to-noise objects (with light-curve parameters described in Section 7.1), five of which have TRGB distances. Of the 18 calibrating SNe Ia used in this study, 13 have non-CSP-I photometry; these have also been analyzed in a consistent manner using SNoPy. The five that have CSP-I photometry are SN 2007af, SN 2007on, SN 2007sr, SN 2011iv, and SN 2012fr. The remaining 99 (out of the sample of 104) SNe Ia form the basis of our distant SN Ia sample. As discussed further in Section 7, calibration of these data and a determination of H_0 based on the Cepheid distances to nearby SN Ia hosts from Riess et al. (2016) are given in Burns et al. (2018). Here we independently determine H_0 using the CSP-I SNe Ia and our new CCHP TRGB distances.

¹⁹ There have been three releases of the CSP-I data: (1) Contreras et al. (2010) published data for 35 SNe Ia, (2) Stritzinger et al. (2011) published data for 50 SNe Ia, and (3) Krisciunas et al. (2017) provided data for the entire CSP-I set of 123 SNe Ia. The CSP-I data are available at <http://csp.obs.carnegiescience.edu/data>.

Table 4
SNe, Hosts, and References

Name	Host	Optical Reference	Near-infrared Reference
SN 1980N	NGC 1365	Hamuy et al. (1991)	Elias et al. (1981)
SN 1981B	NGC 4536	Tsvetkov (1982)	Elias et al. (1981)
SN 1981D	NGC 1316	Walker & Marino (1982)	Elias et al. (1981)
SN 1989B	NGC 3627	Wells et al. (1994)	Wells et al. (1994)
SN 1994D	NGC 4526	Richmond et al. (1995)	Richmond et al. (1995)
SN 1994ae	NGC 3370	Riess et al. (2005)	...
SN 1995al	NGC 3021	Riess et al. (1999)	...
SN 1998bu	NGC 3368	Jha et al. (1999)	Jha et al. (1999)
SN 2001el	NGC 1448	Krisciunas et al. (2003)	Krisciunas et al. (2003)
SN 2002fk	NGC 1309	Silverman et al. (2012)	Cartier et al. (2014)
SN 2006dd	NGC 1316	Stritzinger et al. (2010)	Stritzinger et al. (2010)
SN 2007af	NGC 5584	Stritzinger et al. (2011)	Stritzinger et al. (2011)
SN 2007on	NGC 1404	Gall et al. (2018)	Gall et al. (2018)
SN 2007sr	NGC 4038	Schweizer et al. (2008)	Schweizer et al. (2008)
SN 2011fe	NGC 5457	Richmond & Smith (2012)	Matheson et al. (2012)
SN 2011iv	NGC 1404	Gall et al. (2018)	Gall et al. (2018)
SN 2012cg	NGC 4424	Marion et al. (2016)	Marion et al. (2016)
SN 2012fr	NGC 1365	Contreras et al. (2010)	Contreras et al. (2010)

Type Ia SNe are not perfect standard candles; they require three empirical corrections. The first is a stretch correction, commonly referred to as the Phillips relation (Phillips 1993), which accounts for variations in the amount of radioactive ^{56}Ni synthesized in the explosion and is thought to power the light curve of the SN Ia. Brighter events have more ^{56}Ni but also longer diffusion times in their ejecta, producing a correlation between peak luminosity and the width of the light curve. The second correction uses the less well-understood empirical correlation between the stretch-corrected peak luminosity and galaxy host mass (or metallicity) discussed in Section 6.1. Finally, a correction must be made to account for the extinction due to dust along the line of sight to the SNe Ia.

There are two commonly used ways to deal with extinction for SNe Ia. The first is to assume that the slope of the reddening law R_V (Cardelli et al. 1989; Fitzpatrick 1999) is universal and work with reddening-free magnitudes (Madore 1982), as originally done by Tripp (1998). In this case, the reddening correction is simply a constant, β , multiplied by the observed color of the SNe Ia. The corrected magnitude can then be computed as

$$B' = B - P^1(s_{BV} - 1) - P^2(s_{BV} - 1)^2 - \beta(B - V) - \alpha_M(\log_{10} M_*/M_\odot - M_0), \quad (2)$$

where P^1 is the linear coefficient and P^2 is the quadratic coefficient in $(s_{BV} - 1)$, which encapsulate the Phillips relation; β is the slope of the color correction; B and V are the apparent, K -corrected peak magnitudes; and α_M is the slope of the correlation between peak luminosity and host stellar mass M_* .²⁰ This approach has the advantage of being simple and direct but does not capture the observed diversity in R_V seen in the Milky Way (e.g., Fitzpatrick 1999) and host galaxies of SNe Ia (Mandel et al. 2011; Burns et al. 2014; Nataf 2015). Furthermore, any intrinsic correlation in SN Ia color and luminosity could bias the correction (Mandel et al. 2017). Alternatively, we can use the methods of Burns et al.

²⁰ Host stellar masses are derived as described in Burns et al. (2018), Appendix B.

(2014) to solve explicitly for the dust properties ($E(B - V)$ and R_B) of each SN Ia host. In this case, the corrected magnitude becomes

$$B' = B - P^1(s_{BV} - 1) - P^2(s_{BV} - 1)^2 - R_B E(B - V) - \alpha_M(\log_{10} M_*/M_\odot - M_0), \quad (3)$$

where R_B and $E(B - V)$ are derived from the optical and near-infrared colors of each SN Ia. The disadvantage of this method is that an extra step—determining the intrinsic colors of SNe Ia as a function of $(s_{BV} - 1)$ —must be done, and errors in this step introduce correlated errors in the values of B' , which must be taken into account in determining H_0 . Having made the color-dependent corrections, the apparent magnitudes of the SNe Ia now depend only on their relative distances.

In both cases, the apparent magnitudes at maximum are computed by fitting the light curves with SNooPy (Burns et al. 2011), which yields the time of maximum, the light-curve shape s_{BV} , and the magnitude at maximum for each filter. These are then used as inputs to an MCMC fitter that simultaneously solves for all of the correction factors: P^1 , P^2 , α_M , β , $E(B - V)$, and R_B (for full details, see Burns et al. 2018). Not only does this provide us with the corrected magnitudes, it also gives a full covariance matrix, which is used when determining H_0 and its error.

6.3. Supercal Sample

In comparison to the CSP-I SN Ia sample, we also apply our TRGB calibration to the Supercal sample²¹ (Scolnic et al. 2015). This catalog merges data from five different SN samples (including early CSP-I releases) and references them to a common photometric zero-point, measured relative to the large and uniformly calibrated area of the Pan-STARRS survey.

Our Supercal subsample contains 214 objects with $0.0023 < z < 0.15$. For a direct comparison with previous results, following Betoule et al. (2014) and Riess et al. (2016), we impose a number of cuts on the Supercal sample by including

²¹ <http://kicp.uchicago.edu/~dscolnic/supercal/supercal.fits>

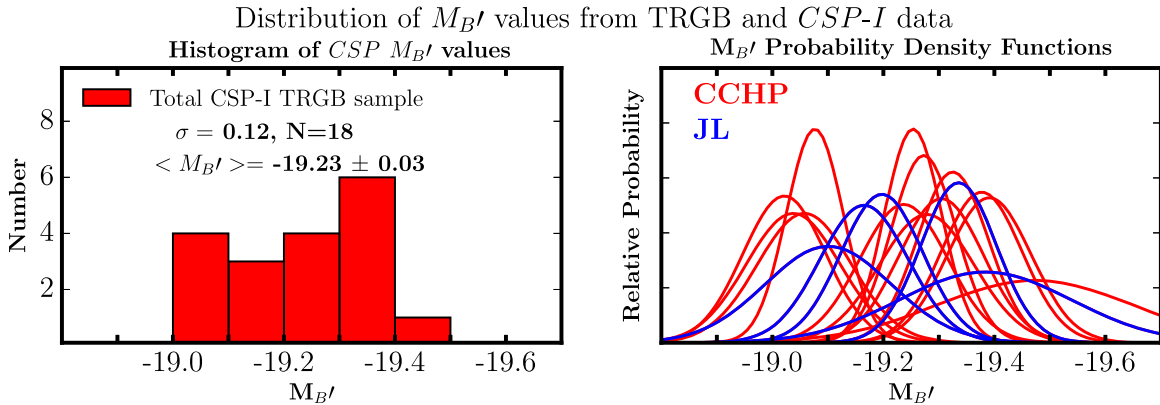


Figure 8. Tripp B' -band absolute magnitude distributions for TRGB calibrators for the CSP-I sample in histogram form (left panel) and probability density functions (right panel). Shown in the left panel are the weighted mean values for $M_{B'}$, the dispersion, the number of galaxies, and the error on the mean. In the right panel, the galaxies analyzed by Jang & Lee (2017a) are shown in blue.

only SN Ia light curves for which the SALT color parameter (c) is within ± 0.3 ; restricting the light-curve parameter (x) to be within ± 3.0 ; and requiring the χ^2 of the light-curve fit to be good ($\text{fitprob} > 0.01$), where the peak time of the light curve is constrained to better than 2 days and the uncertainty in the corrected peak magnitude is < 0.2 mag. As described in Scolnic et al. (2015, 2018), the SN Ia redshifts were corrected using a flow model based on the observed nearby matter density.²² In addition, they found and included a residual peculiar velocity error of ± 250 km s $^{-1}$. For the 214 SNe Ia in our cut sample, we find an intercept in the magnitude–redshift diagram of $a_B = 0.71639$ (for comparison, Riess et al. 2016 found an intercept of 0.71273 for a sample of 217 SNe Ia).

6.4. Absolute Magnitude Distribution of the Calibration SNe Ia

To recap briefly, our TRGB sample consists of 18 calibrating SNe Ia, and the Cepheid sample consists of 19 calibrating SNe Ia. Ten of these SNe Ia have both TRGB and Cepheid distances.

The accuracy of the H_0 measurement rests on the accuracy with which the average absolute magnitude, $M_{\lambda,i}$, can be determined,

$$M_{\lambda,i} = m_{\lambda,i} - \mu_{0,i}^{\text{TRGB/Ceph}}, \quad (4)$$

where λ is the filter of the observation, i is the subsample of SNe Ia for that filter, $m_{\lambda,i}$ is the apparent magnitude of the peak of the SN Ia light curve for a given filter, and μ_0 is the true calibrator distance modulus (TRGB or Cepheid).

In Figure 8, we show the distribution of $M_{B'}$ magnitudes of the TRGB calibrators for the CSP-I (SNooPY-analyzed) sample of 18 SNe Ia in both histogram form (left panel) and probability density functions (right panel). In the right panel, the galaxies analyzed in this paper are shown in red, and those by Jang & Lee (2017a) are shown in blue. The CSP-I apparent peak B' magnitudes are defined in Equation (2) and listed in column 6 of Table 3; the TRGB distance moduli are given in column 3. The average weighted mean magnitude for this sample is $M_{B'}[N=18] = -19.225$ mag with a dispersion of ± 0.119 mag and an error on the mean of ± 0.029 mag. The individual uncertainties in $M_{B'}$ are given by

$\sigma = \sqrt{\sigma_{\text{SN}}^2 + \sigma_{\text{TRGB}}^2}$. The relative weight (calculated as $1/\sigma^2$) for an individual SN is determined by the uncertainty in both its SN photometry, σ_{SN} , and TRGB distance, σ_{TRGB} ; these uncertainties can be seen in the right panel. The three objects with the lowest weights for this sample are SN 1981D in NGC 1316, SN 2007sr in NGC 4038, and SN 2007af in NGC 5584. A series of jackknife tests show that the mean is very stable, and the difference between the weighted and unweighted means is only 0.013 mag (0.6%). The results are very similar whether or not the two reddest objects (the Leo Group galaxies, NGC 3627 and NGC 3368) are excluded from the sample (the weighted mean changes by only 0.004 mag, or 0.2%), and removing the transitional objects, SN 2007on and SN 2011iv, in NGC 1404 does not change the weighted mean. For the 10 SNe Ia for which there are both Cepheid and TRGB distances, $M_{B'}[N=10] = -19.239$ mag, with a dispersion of ± 0.093 mag and an error on the mean of ± 0.031 mag, amounting to a difference of 0.6% from that for the total sample of 18 galaxies.

We next look at the SHoES sample of calibrators. We note that the CSP-I B' -band magnitudes (defined in Equation (2)) cannot be compared directly with those from Riess et al. (2016, 2019), since they are defined differently.²³ Rather, the discussion below is intended to be illustrative of where some of the differences arise in the ultimate measurement of H_0 . These differences arise from a number of factors, including differences in calibration, SN Ia calibrator samples, and uncertainties.

In Figure 9, we show the SN Ia M_B absolute magnitude distributions ($M_{B,i} = m_{B,i} - \mu_{0,i}^{\text{TRGB/Ceph}}$) based on the SHoES SN Ia data for various subsets of the TRGB and Cepheid calibrating galaxy samples. In this figure, the absolute magnitudes were calculated based on the apparent SN Ia m_b^{max} magnitudes listed in column 6 of Table 3 (from Riess et al. 2016, Table 5), the Cepheid distance moduli listed in column 8 of Table 3 (also from Riess et al. 2016, Table 5), and the TRGB distance moduli from the present paper listed in column 3 of Table 3. We update these distance moduli from the Riess et al. (2016) to the Riess et al. (2019) magnitude scale. The Riess et al. (2016) distances and H_0 values are tied to three anchors, the Milky Way, NGC 4258, and the LMC, which

²² <http://cosmicflows.iap.fr/>

²³ There are 19 SNe Ia that have both $m_{B'}^{\text{CSP}}$ and m_B^{SC} magnitudes (see Table 3). The mean difference is 0.061 mag with a standard deviation of 0.102 mag.

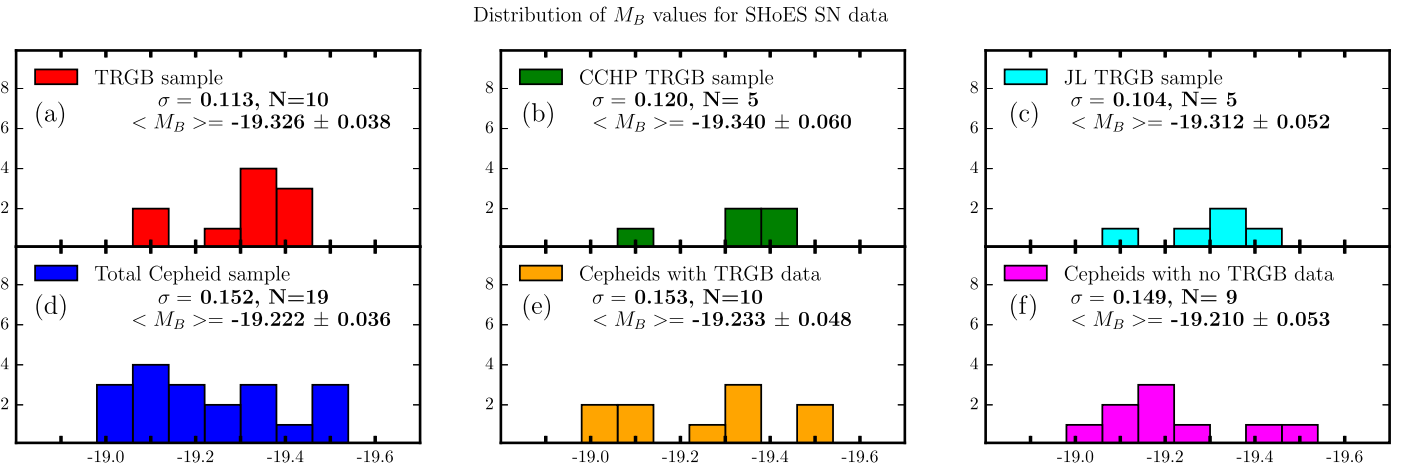


Figure 9. The B -band absolute magnitude distributions based on the *SHoES* SN Ia data from Riess et al. (2016) and updated to the recalibration by Riess et al. (2019) for different subsamples of the calibrating galaxy samples. Figures 9(a)–(c) show the M_B histograms based on TRGB distances for (a) the 10 galaxies having both Cepheid and TRGB distances, (b) the subset of five CCHP TRGB distances, and (c) the remaining subset of five TRGB galaxies measured by Jang & Lee (2017a). Figures 9(d)–(f) show the histograms based on the Riess et al. (2016, 2019) Cepheid distances for (d) their full sample of 19 galaxies, (e) the overlap sample of 10 galaxies having measured Cepheid and TRGB distances, and (f) the nonoverlap sample of galaxies with Cepheid distances but no TRGB distances. Shown in the plots are the weighted mean values for M_B , the dispersion, the number of galaxies, and the error on the mean. We note that the dispersion in the TRGB calibration of the SNe Ia is significantly smaller ($\sigma = \pm 0.10\text{--}0.12$) than that for the Cepheid calibrators ($\sigma = \pm 0.15$) and is the same as that for the far-field dispersion of 0.1 mag.

resulted in a value of $H_0 = 73.24 \text{ km s}^{-1} \text{ Mpc}^{-1}$. For the purpose of comparison in calculating $M_{B,i}$ values, we compare the TRGB and Cepheid distances and H_0 values anchored to the LMC alone. The Riess et al. (2019) H_0 value for the LMC alone is $74.22 \text{ km s}^{-1} \text{ Mpc}^{-1}$, a difference of $5\log^{10}(73.24/74.22) = -0.029$ mag. In Figures 9(d)–(f), this difference is added to the Cepheid moduli from Table 3.

Figures 9(a)–(c) show the M_B histograms based on TRGB distances for (a) the 10 galaxies having measured Cepheid and TRGB distances, (b) the subset of five CCHP TRGB distances, and (c) the remaining subset of five TRGB galaxies measured by Jang & Lee (2017a). The weighted mean absolute M_B magnitudes are all consistent to within the quoted errors; these values are displayed in each of the panels, along with the standard deviations, σ , and numbers of objects, N . Figures 9(d)–(f) show the histograms based on the Riess et al. (2016) Cepheid distances for (d) their full sample of 19 galaxies, (e) the overlap sample of 10 galaxies having measured Cepheid and TRGB distances, and (f) the nonoverlap sample of galaxies with Cepheid distances but no TRGB distances. The weighted mean absolute M_B magnitudes are again all internally consistent to within the quoted errors, labeled in each of the panels. However, for the sample of 10 overlapping galaxies (panels (a) and (e)), the TRGB (-19.326 ± 0.038 mag) and Cepheid (-19.233 ± 0.048 mag) calibrations of M_B differ by 0.104 mag (4.4% in distance). These values diverge as a result of the combination of differences in (1) zero-point calibration, (2) the relative weightings of TRGB and Cepheid distances, (3) the full sample of 19 galaxies compared to the overlap sample of 10 galaxies, and (4) the SN Ia apparent B magnitudes.

7. Determination of the Hubble Constant

We now apply our TRGB calibration to the CSP-I SN Ia sample and determine a value for H_0 using an MCMC method. We test the robustness of this value by examining different subsets of the calibrators and distant SN Ia data sets. We list the values of H_0 for these different samples in Table 5. In

Section 7.3 we apply our TRGB calibration to the Supercal SN Ia sample. We compare the TRGB and Cepheid calibrations for both the CSP-I and Supercal far-field SN Ia samples. Finally, we return to a discussion of Table 6 in the context of our overall error budget in Section 7.4.

7.1. TRGB Calibration of the CSP-I SN Ia Sample

In this section, we use the measured TRGB distances to our sample of 18 nearby SN Ia calibrators, described above and listed in Table 3, and apply this zero-point calibration to the far-field CSP-I sample of SNe Ia. References for the SN photometry for the TRGB calibrating sample are given in Table 4; these SNe Ia have been analyzed using SNooPy, consistent with the distant CSP-I sample. We focus our analysis on the sample of SNe Ia with $s_{\text{BV}} > 0.5$ and $E(B - V) < 0.5$ mag, avoiding the reddest and fastest decliners, of which there are 18 (10 with $s_{\text{BV}} < 0.5$ and eight with $E(B - V) > 0.5$ mag). The observed B magnitudes are modeled with Equation (2), where $\mu = \mu(z, H_0)$ for the distant sample, $\mu = \mu_{\text{TRGB}}^0$ for the nearby calibrators, and H_0 is treated as a free parameter. An intrinsic error term, σ^2 ; a peculiar velocity term; and a zero-point error for the non-CSP-I photometry have all been added in quadrature with the individual galaxy statistical errors from Table 3. We carried out the analysis both with and without a host-galaxy mass correction, as described in detail in Burns et al. (2018).

As in Freedman et al. (2009), we use a simple Taylor series expansion to derive the luminosity distance and the distance modulus as a function of redshift (Caldwell & Kamionkowski 2004; Visser 2004). This kinematic model parameterization is independent of theoretical assumptions about the dark matter and energy content of the universe. The first- and second-order terms in this expansion are parameterized by the deceleration parameter, $q_0 = -\frac{\ddot{a}a}{\dot{a}^2}$, and the cosmic jerk, $j_0 = -\frac{\ddot{\ddot{a}}a^2}{\dot{a}^3}$, which is the third derivative of the scale factor. The luminosity

Table 5
Best-fit Values of H_0 in $\text{km s}^{-1} \text{Mpc}^{-1}$

Filters	Tripp				$E(B - V)$				N_{calib}
	H_0 (HM)	σ	H_0 (noHM)	σ	H_0 (HM)	σ	H_0 (noHM)	σ	
Full Sample									
<i>B</i>	69.70	1.41	70.32	1.32	70.63	1.34	71.22	1.29	18
<i>i</i>	69.00	1.30	69.73	1.23	68.90	1.36	69.56	1.32	16
<i>J</i>	69.56	1.36	69.98	1.35	69.78	1.51	70.14	1.48	16
<i>H</i>	69.21	1.35	69.69	1.30	69.46	1.44	69.88	1.40	16
$s_{\text{BV}} > 0.5$									
<i>B</i>	69.65	1.37	70.13	1.31	70.42	1.18	70.91	1.19	18
<i>i</i>	68.92	1.27	69.54	1.21	68.85	1.32	69.43	1.29	16
<i>J</i>	69.43	1.34	69.74	1.32	69.59	1.49	67.97	1.44	16
<i>H</i>	69.21	1.33	69.66	1.32	69.46	1.43	69.88	1.39	16
$E(B - V) < 0.5$									
<i>B</i>	69.67	1.34	70.28	1.28	70.16	1.33	70.85	1.27	18
<i>i</i>	69.00	1.30	69.68	1.22	68.43	1.36	69.30	1.32	16
<i>J</i>	69.46	1.36	69.72	1.35	69.28	1.50	69.69	1.48	16
<i>H</i>	69.12	1.34	69.55	1.32	68.90	1.48	69.47	1.41	16
$E(B - V) < 0.25$									
<i>B</i>	68.83	1.42	69.48	1.34	70.77	1.43	71.42	1.36	15
<i>i</i>	68.70	1.41	69.58	1.32	69.21	1.48	70.03	1.41	13
<i>J</i>	69.79	1.48	70.16	1.46	70.20	1.64	70.51	1.56	13
<i>H</i>	69.79	1.49	70.21	1.47	69.82	1.60	70.29	1.56	13
$s_{\text{BV}} > 0.5$ and $E(B - V) < 0.5$									
<i>B</i>	69.67	1.35	70.27	1.29	69.88	1.17	70.46	1.18	18
<i>i</i>	68.98	1.29	69.66	1.21	68.35	1.30	69.09	1.25	16
<i>J</i>	69.45	1.36	69.70	1.35	69.10	1.48	69.46	1.46	16
<i>H</i>	69.15	1.35	69.57	1.32	68.87	1.45	69.39	1.42	16

Table 6
Summary of H_0 Uncertainties

Source of Error	Random Error	Systematic Error	Description
LMC zero-point	1.0%	1.8%	Section 3.4
CSP-I SNe Ia	0.5%	1.8%	Section 7.1
Total	1.1%	2.5%	In quadrature

distance can then be written as

$$d_L(z, z_{\text{hel}}, H_0, q_0, j_0) = \frac{(1 + z_{\text{hel}})cz}{(1 + z)H_0} \left\{ 1 + \frac{1}{2}[1 - q_0]z - \frac{1}{6}[1 - q_0 - 3q_0^2 + j_0]z^2 \right\}. \quad (5)$$

Our redshifts are sufficiently small that the third-order j_0 term is unimportant. We assume a flat cosmology, $\Omega_k = 0$, with $q_0 = \Omega_m/2 - \Omega_{DE} = -0.53$, where $\Omega_m = 0.315$ (Planck Collaboration et al. 2018). The distance modulus is then given by

$$\mu(z, H_0, q_0) = 5 \log_{10} \left\{ \frac{(1 + z_{\text{hel}})cz}{(1 + z)H_0} \left(1 + \frac{1 - q_0}{2}z \right) \right\} + 25. \quad (6)$$

In Table 5, we present a summary of the values of H_0 derived from the Tripp and explicit reddening-corrected magnitudes individually for each of the *BiJH* CSP-I filters. We separately analyze the cases where there is a correction for host mass (HM) and no correction (noHM) for different color and stretch constraints as labeled. Also listed, in the final column, is the number of calibrating SNe Ia observed in each

filter. The tabulated uncertainties are those determined from a diagonal covariance matrix with respect to the TRGB distances.

For the $(B - V)$ color-corrected Tripp *B*-band analysis with $s_{\text{BV}} > 0.5$ and $E(B - V) < 0.5$, we find $H_0 = 69.67 \pm 1.35$ and $70.27 \pm 1.29 \text{ km s}^{-1} \text{ Mpc}^{-1}$ with and without the mass correction, respectively. For the explicit reddening-correction ($E(B - V)$) model, we find $H_0 = 69.88 \pm 1.17$ and $70.46 \pm 1.18 \text{ km s}^{-1} \text{ Mpc}^{-1}$, respectively, with all values agreeing well to within their quoted uncertainties (see Table 5).

Burns et al. (2018) found that the largest source of systematic error for the SNe Ia was the difference in average host-galaxy stellar mass between the Riess et al. (2016) Cepheid sample and the more distant CSP-I sample. In that case, the limited mass range of the calibrating sample introduced a covariance between H_0 and α_M . It limited the precision with which α_M could be estimated, in turn increasing the overall H_0 systematic error, unlike the case for the TRGB sample. The agreement cited in the paragraph above underscores the additional advantage of this analysis in that the galaxy host masses of the TRGB sample are more massive, on average, than the Cepheid sample, making the TRGB set a good match to the CSP-I distant sample.

Based on this MCMC analysis, our adopted best value for H_0 is $69.8 \pm 1.3 \text{ km s}^{-1} \text{ Mpc}^{-1}$. This value is obtained using the *B*-band photometry, for which the largest number of calibrators is available, and by conservatively restricting the sample to SNe Ia that are not fast decliners ($s_{\text{BV}} > 0.5$) or highly reddened ($E(B - V) < 0.5$); allowing for a host-mass correction; and averaging the values from the Tripp derivation ($H_0 = 69.67 \pm 1.35 \text{ km s}^{-1} \text{ Mpc}^{-1}$) and the explicit $E(B - V)$ reddening correction ($H_0 = 69.88 \pm 1.17 \text{ km s}^{-1} \text{ Mpc}^{-1}$). We note that most of the values within this table fall within 1σ of our adopted value, despite differences in sample size,

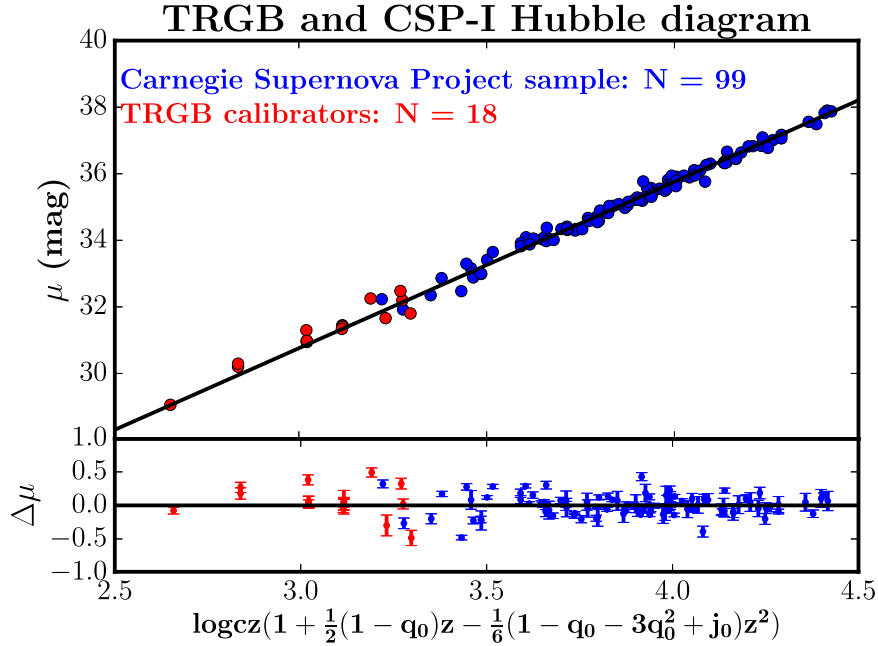


Figure 10. Hubble diagram for 99 SNe Ia observed as part of the CSP-I (blue squares). Also shown are the TRGB calibrators (this paper; red circles). A slope = 5 line is plotted. The TRGB velocities have been corrected as described in Section 5.

wavelength, and whether or not a host-mass correction is applied. Most of the outliers occur at wavelengths where there are only a small number of calibrators. We note that a direct reddening correction results in a decrease of the uncertainty in the B -band solution, while the uncertainty increases in the case of the redder JH bands.

The systematic errors in the zero-point have been listed separately in Table 2. We combine in quadrature the systematic error for the zero-point with that from the SN Ia analysis to give the total uncertainty in H_0 . The final adopted errors are summarized in Table 6 of Section 7.2 below. Our adopted value of the Hubble constant and its uncertainty, as derived from the TRGB method applied to the CSP-I sample of SNe Ia, then becomes $H_0 = 69.8 \pm 0.8$ (stat) ± 1.8 (sys) $\text{km s}^{-1} \text{Mpc}^{-1}$.

7.2. The Hubble Diagram

In Figure 10, we show the Hubble diagram for the 18 TRGB calibrating galaxies (red filled circles) at low redshift connecting to the CSP-I sample of 99 SNe Ia (blue filled squares) extending out to $z = 0.08$. The distance moduli are computed from Tripp B magnitudes for SNe Ia with $s_{BV} > 0.5$ and $E(B - V) < 0.5$. A host-mass correction has been applied. Residuals from the fit in distance modulus are shown in the bottom panel. This figure illustrates the major result of this paper: a new and completely independent calibration of H_0 based on the TRGB and CSP-I SNe Ia.

In Figure 11, the nearby TRGB calibrators are shown in more detail. The points are labeled by galaxy name in the Hubble diagram shown in the top panel and by SN name in the bottom panel showing the residuals from the Hubble diagram. A line with a slope of 5 is shown in the top panel.

The distribution of H_0 values calculated for each of the individual SNe Ia is shown in Figure 12. The individual H_0 values and their 1σ uncertainties are plotted for the 99 CSP-I SNe Ia as individual Gaussians in blue. The black line is the summed and scaled probability density function. In Figure 13, the same H_0 values are shown in histogram form.

Our result agrees to within 1.3σ of the combined uncertainties with that of Burns et al. (2018; accounting for the new Pietrzynski 2019 LMC calibration), who obtained a value of $H_0 = 73.2 \pm 2.3 \text{ km s}^{-1} \text{ Mpc}^{-1}$. In Burns et al. (2018), the CSP-I data were calibrated with the published Cepheid distances from Riess et al. (2016) but independently analyzed, and they resulted in a larger estimated uncertainty for H_0 than obtained by Riess et al. (2016).

7.3. Comparison with the Supercal Sample

In Figure 14, we show a combined Hubble diagram including the CSP-I sample of 99 SNe Ia (blue filled circles) from Burns et al. (2018) superimposed on the Supercal sample of 214 galaxies (light blue open circles) from Scolnic et al. (2015) with $0.023 < z < 0.15$, as described in Section 6.3. Plotted is $0.2m_b^{\max}$ (where m_b^{\max} is the apparent B magnitude of the SN Ia at maximum luminosity) versus redshift. This comparison illustrates the high quality of the CSP-I sample photometry.

Applying our TRGB zero-point calibration to the Supercal SN Ia sample, we find a value of $H_0 = 70.4 \pm 1.4 \text{ km s}^{-1} \text{ Mpc}^{-1}$ (not including the systematic uncertainty). This estimate is based on the 10 SNe Ia in Table 5 of Riess et al. (2016) for which there is B -band SN Ia photometry and we have TRGB distances.²⁴ This value can be directly compared with the published value of $H_0 = 74.22 \pm 1.82 \text{ km s}^{-1} \text{ Mpc}^{-1}$ from Riess et al. (2019), using only the LMC as an anchor galaxy. In both cases, the recent Pietrzynski (2019) distance modulus of 18.477 mag to the LMC has been adopted. (For comparison, the older Riess et al. 2016 calibration used the Pietrzynski et al. 2013 distance modulus to the LMC of 18.493 mag and obtained an LMC-only anchored value of $H_0 = 72.04 \pm 2.56 \text{ km s}^{-1} \text{ Mpc}^{-1}$.) This new LMC distance modulus contributes 0.7% (0.016 mag) to the 3% difference between the Riess et al. (2016, 2019) LMC-anchored values of H_0 . The dominant contribution to the

²⁴ For the sample of 19 Cepheid galaxies, we find $H_0 = 73.83 \text{ km s}^{-1} \text{ Mpc}^{-1}$.

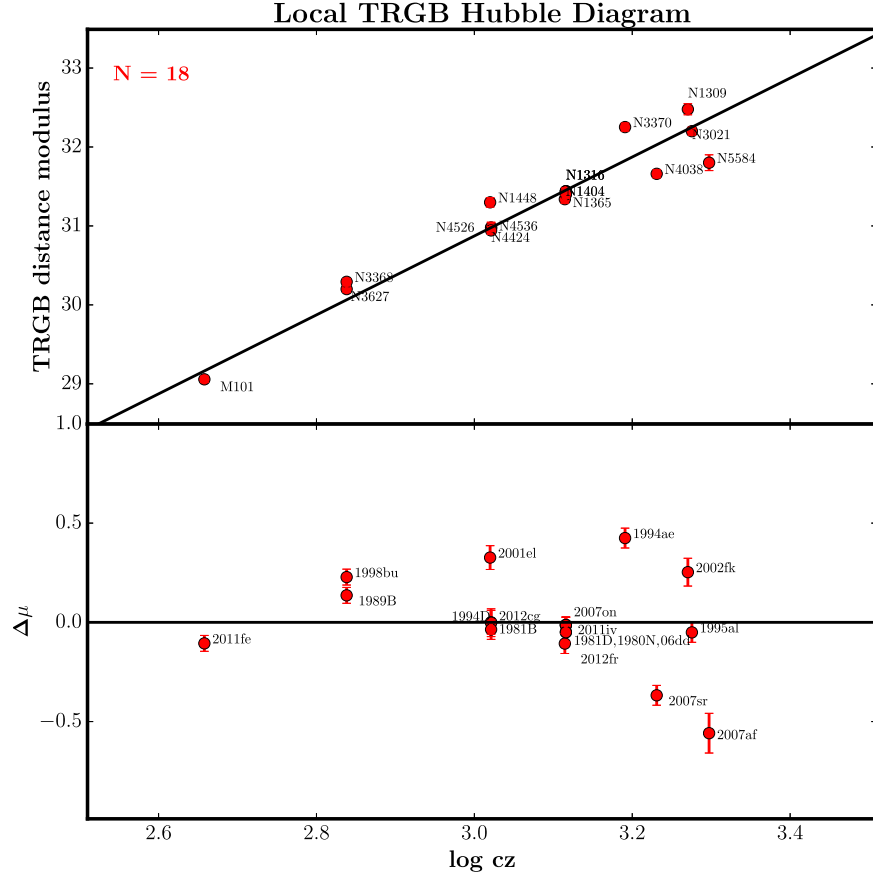


Figure 11. Top panel: Hubble diagram for the total sample of 18 TRGB calibrators, where each point is labeled by its host-galaxy name. The slope is determined from the distant CSP-I sample of 99 galaxies. Bottom panel: residuals from the Hubble diagram. Each point is labeled by its SN name. Once again, the velocities have been corrected using the NED nearby galaxies mass model.

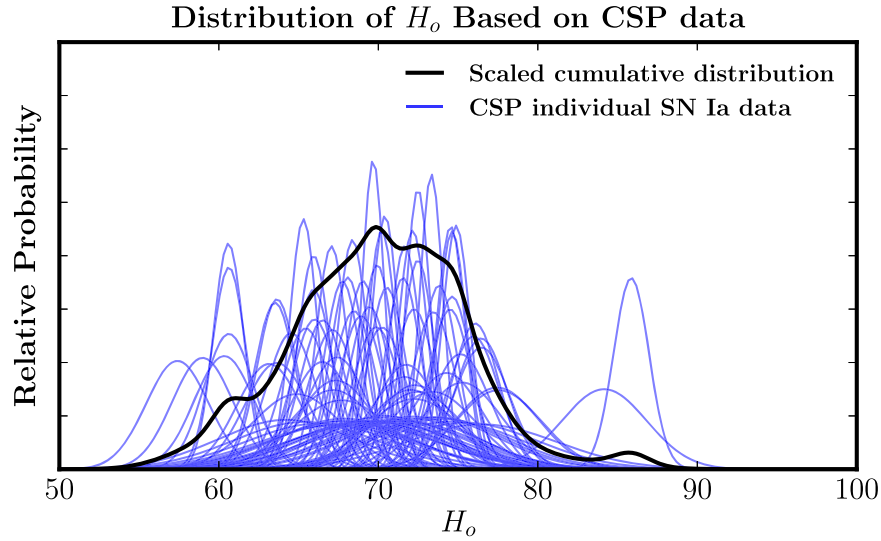


Figure 12. Probability distribution functions for the individual values of H_0 calculated for each CSP-I SN Ia are shown in blue. The summed and scaled probability density function is shown in black.

difference comes from the Riess et al. (2019) recalibration of the WFC3 photometry for the LMC Cepheids.

The distribution of H_0 values from the Supercal data is shown in Figure 15. The H_0 values and 1σ uncertainties for the 214 Supercal SNe Ia are plotted as individual Gaussians in blue. A scaled and summed probability density function is

given by the black line. In Figure 16, the H_0 values are shown in histogram form.

7.4. Summary of H_0 Results

As described in Section 7.1, our best value of the Hubble constant, based on the TRGB distances to 18 SNe Ia anchored

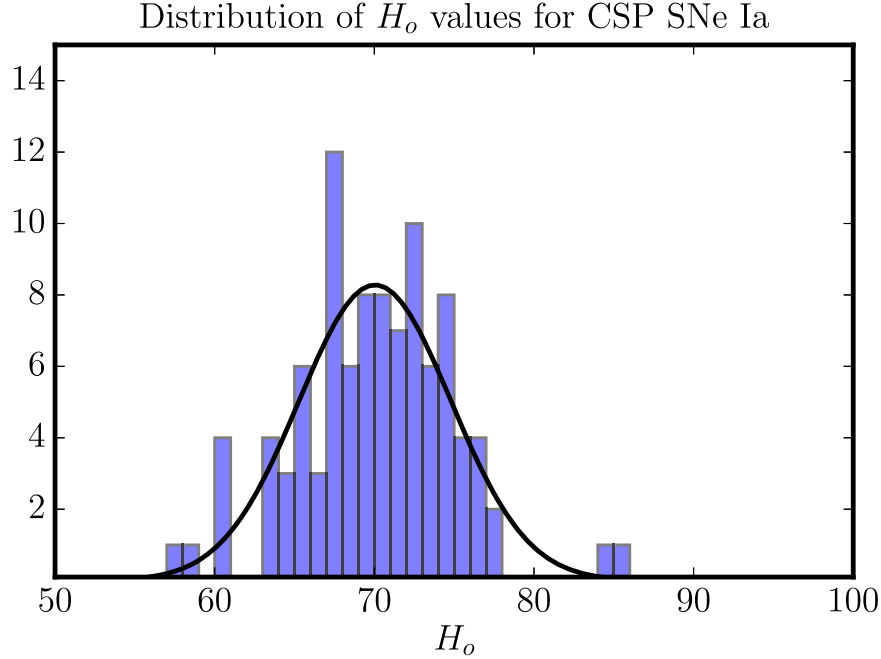


Figure 13. Histogram of H_0 values for the individual 99 SNe Ia observed as part of the CSP-I, calibrated by the TRGB distances from this paper.

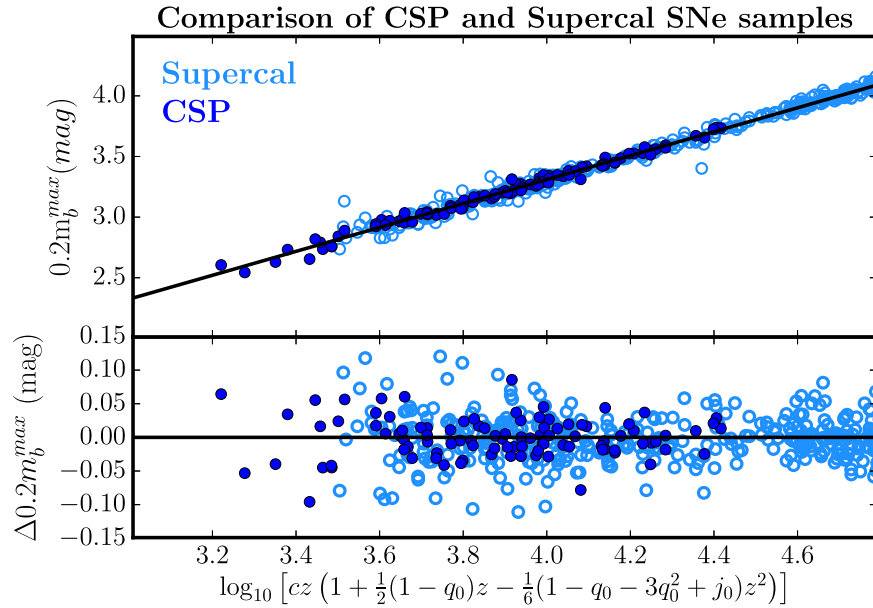


Figure 14. Top panel: Hubble diagram for 99 SNe Ia observed as part of the CSP-I (blue filled circles). Shown also is the Supercal sample of 214 SNe Ia (light blue open circles). The two data sets have been arbitrarily set to the same zero-point for comparison purposes only. Bottom panel: residuals from the Hubble diagram above. Colors remain the same as above.

to 99 CSP-I distant SNe Ia and determined via an MCMC analysis, results in a value of $H_0 = 69.8 \pm 0.8$ (stat) ± 1.7 (sys) $\text{km s}^{-1} \text{Mpc}^{-1}$.

Our result differs from the best value of $H_0 = 74.03 \pm 1.42 \text{ km s}^{-1} \text{Mpc}^{-1}$ from Riess et al. (2019) for a number of reasons. These include the zero-point calibration, as well as different subsamples of galaxies that contribute to the determination of the absolute SN Ia magnitudes, uncertainties for individual galaxy distances and SN Ia photometry (and therefore different weightings), SN Ia samples (CSP-I versus Supercal), treatment of SN Ia host-galaxy mass, and analysis methods (MCMC versus a maximum likelihood/matrix

inversion approach). The difference (at the 1.7σ level) suggests that further work is necessary to reduce the remaining systematic uncertainties.

7.5. Comparison with Other Recent Measurements of the Hubble Constant

Recent measurements of the local expansion rate have been made based on a number of alternative methods, including strong gravitational lensing (Suyu et al. 2017; Birrer et al. 2018), the Tully–Fisher relation using the TRGB (Mould & Sakai 2008) or Cepheids (Sorce et al. 2013), and the optical

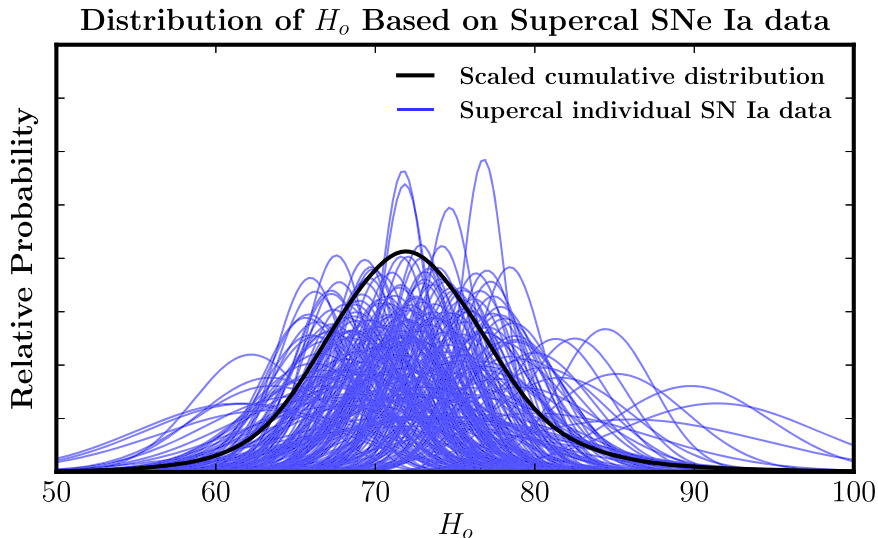


Figure 15. Probability distribution functions for the individual values of H_0 calculated for each Supercal SN Ia are shown in blue. The scaled and summed probability density function is shown in black.

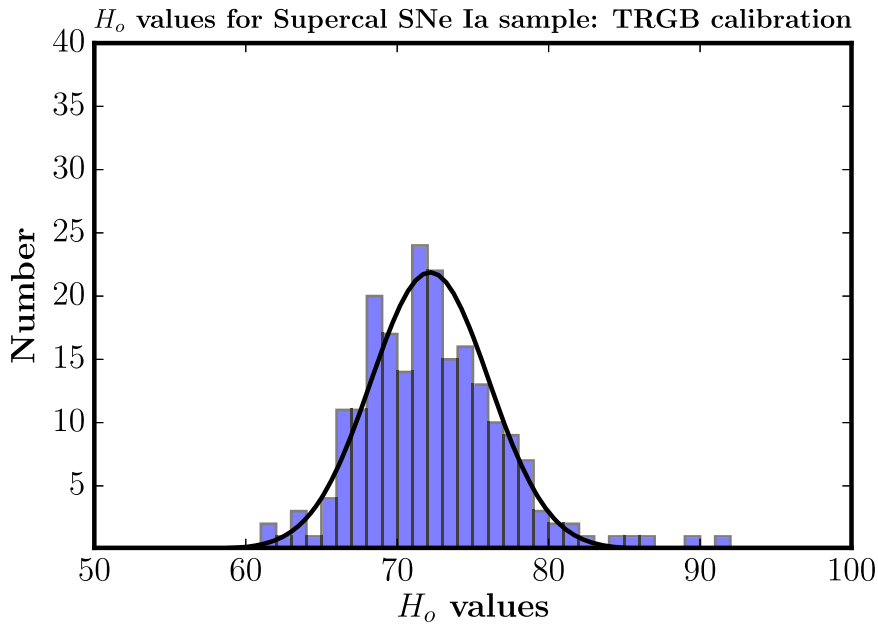


Figure 16. Histogram of H_0 values for the individual 214 SNe Ia observed as part of Supercal, calibrated by the TRGB distances from this paper.

counterpart to GW170817 (Abbott et al. 2017), in addition to the Cepheid calibration of SNe Ia (Riess et al. 2011; Freedman et al. 2012; Riess et al. 2016; Burns et al. 2018). All of these studies find H_0 values in the range of $70\text{--}74 \text{ km s}^{-1} \text{ Mpc}^{-1}$, with individual uncertainties quoted in the 3%–10% ($2\text{--}7 \text{ km s}^{-1} \text{ Mpc}^{-1}$) range. None of them meaningfully overlap the Planck result. We also note that none of them fall on the low side of the Planck result, as would be expected if they were randomly sampled measurements and the Planck H_0 value were the “true” H_0 value.

A number of reanalyses of the Cepheid/SN Ia data from Riess et al. (2011, 2016) have also been carried out (Efstathiou 2014; Feeney et al. 2017; Zhang et al. 2017). The Zhang et al. (2017) study differs in approach from the other studies in that it was carried out blinded. The starting point for

these analyses, in all cases, is the *HST* Cepheid sample reduced by Riess et al. (2016, and references therein). The Burns et al. (2018) study also uses the Riess et al. (2016) Cepheid distances for its zero-point calibration. The recent analyses of Zhang et al. (2017), Feeney et al. (2017), and Burns et al. (2018) all utilize a Bayesian MCMC approach to estimate the uncertainties in H_0 . Although differing in their details, the conclusion of all of these studies is that the covariance among the multiple parameters in the MCMC analyses is actually very small, with a single exception: that of the distances to the nearby calibrators (the Milky Way, NGC 4258, M31, and the LMC), which set the zero-point (e.g., Feeney et al. 2017; Zhang et al. 2017). This conclusion highlights the (simple and obvious) point that can be made without any formal reanalysis: the values of H_0 move in lockstep with the adopted zero-point of the Leavitt law.

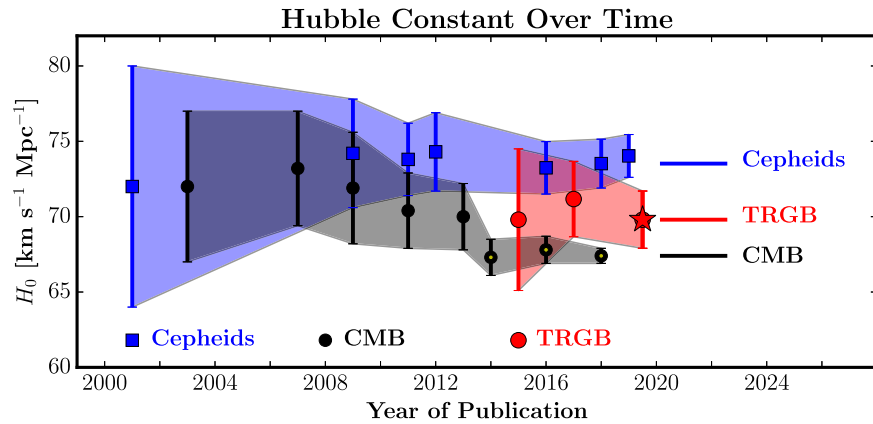


Figure 17. Plot of H_0 values as a function of time. The black points and shaded region are determined from measurements of the CMB, those in blue are Cepheid calibrations of the local value of H_0 , and those in red are TRGB calibrations. The red star is the best-fit value obtained in this paper. Error bars are 1σ .

7.6. Comparison of H_0 Values for Cepheids, TRGB, and Planck

We show in Figure 17 a comparison of local Cepheid (blue) and TRGB (red) determinations of H_0 , as well as values based on CMB measurements (black), plotted as a function of year of publication. The value of H_0 determined in this paper is denoted by a red star and falls between the values defining the current H_0 tension. It favors neither method and can be equally used to argue for evidence that there is no tension (but ignoring the Cepheid results) or that, combining the TRGB and Cepheid results, it provides low-level additional evidence that there is tension between the local and CMB values of H_0 .

8. The Future

In the next few years, a number of ongoing studies will help to sharpen the current debate over the early-universe and locally determined values of H_0 . We list five of them here.

1. A major improvement to the parallax measurements from *Gaia* is expected in 2022. At that time, accurate parallaxes ($\ll 1\%$) will become available for both Milky Way TRGB stars and Cepheids. In addition, they will be available for RR Lyrae stars. Although fainter than TRGB stars or Cepheids, RR Lyrae stars can provide a completely independent zero-point for the nearest galaxies, allowing further testing for hidden systematics.
2. The *HST* will continue to allow measurement of distances to galaxies containing TRGB stars and Cepheids that are host to SNe Ia, thereby increasing the numbers of SN Ia calibrating galaxies. Already, additional *HST* time has been awarded for both programs in Cycle 26 (Proposal 15640, PI: Freedman; Proposal 15642, PI: Riess).
3. The launch of the *JWST* in 2021 will allow TRGB stars to be measured at infrared wavelengths, where these stars are brighter than they are in the optical, thereby increasing the volume out to which TRGB distances can be measured and increasing the number of SN Ia calibrating galaxies. Increasing the number of calibrators is particularly important. As the uncertainty in the zero-point is decreased, the small number of calibrators (and their dispersion in absolute magnitudes) will become the largest uncertainty in the local determination of H_0 . Unfortunately, *JWST* will not be capable of significantly extending the reach of the Cepheid distance scale for a number of reasons: Cepheids are bluer stars, and their

maximum variability (discovery potential) occurs at optical wavelengths. The *JWST*, optimized for the infrared, is diffraction-limited at $2\ \mu\text{m}$. At larger distances, crowding of Cepheids by RGB and brighter AGB stars at redder wavelengths, combined with the smaller amplitudes in the infrared, will severely limit their discovery and ultimate accuracy in H_0 .

4. With Advanced LIGO and Virgo, the expected detection of significant numbers of gravitational-wave events for neutron star–neutron star coalescing binaries may provide a Hubble constant to 2% accuracy within 5 yr (Chen et al. 2018); see, however, Shafieloo et al. (2018), who noted that the accuracy for this method in the near-term will still be dependent on the adoption of an underlying cosmological model.
5. The use of strong gravitational lens systems for measuring H_0 will provide a completely independent measure of H_0 and shows promise for a 1% determination of H_0 in future years as hundreds, and possibly thousands, of time-delay lens systems are discovered in future surveys (e.g., the H0LiCOW program; Suyu et al. 2017).

9. Summary

The major result from this paper is the construction and calibration of a new and independent distance scale for the local universe using the TRGB method, calibrating the absolute distances to SNe Ia in several independent surveys. We determine a value of the Hubble constant of $H_0 = 69.8 \pm 0.8 (\pm 1.1\text{ stat}) \pm 1.7 (\pm 2.4\text{ sys}) \text{ km s}^{-1} \text{ Mpc}^{-1}$. This value differs only at the 1.2σ level from the most recent Planck Collaboration et al. (2018) inferred value of H_0 . It is smaller than previous estimates of the Cepheid calibration of SNe Ia (Freedman et al. 2012; Riess et al. 2019) but still agrees well at the 1.7σ level. The TRGB method provides an opportunity to test for systematics in the Cepheid-based determination of H_0 , which is significantly discrepant with that inferred from Planck. As we have demonstrated, the precision of the TRGB method is high, and future near-term improvements will continue to increase its accuracy.

In Figure 18, we compare the H_0 probability density distributions for the TRGB, calibrated with the distance to the LMC, and Cepheids, calibrated with Milky Way parallax distances and the maser distance to NGC 4258 (and excluding the LMC calibration for Cepheids). Riess et al. (2019) determined

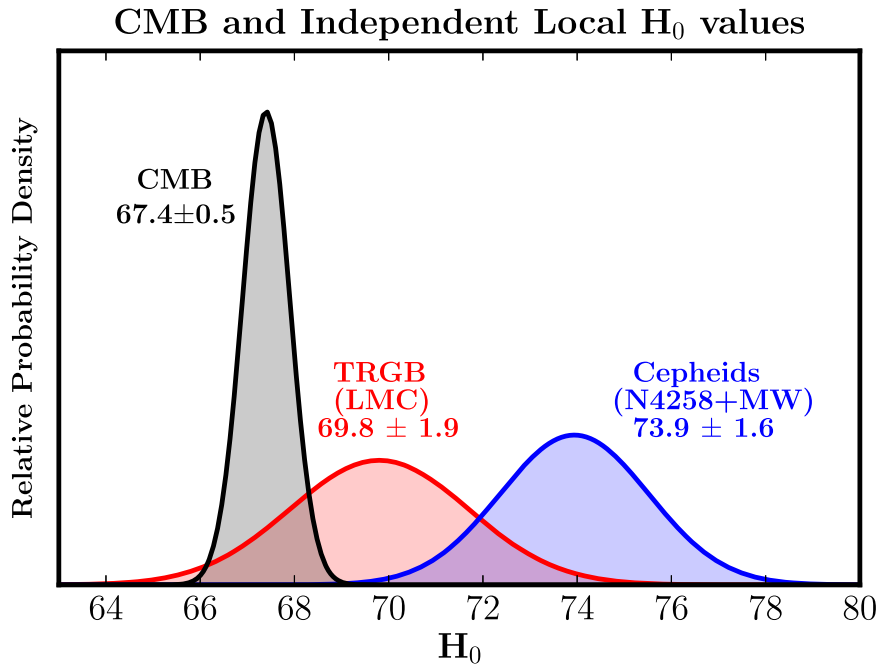


Figure 18. Completely independent calibrations of H_0 . Shown in red is the probability density function based on our LMC CCHP TRGB calibration of CSP-I SNe Ia; in blue is the Cepheid calibration of H_0 (Riess et al. 2016) using the Milky Way parallaxes and maser distance to NGC 4258 as anchors (excluding the LMC). The Planck value of H_0 is shown in black.

a value of $H_0 = 73.94 \pm 1.58 \text{ km s}^{-1} \text{ Mpc}^{-1}$ based on the Milky Way and NGC 4258 calibration alone. This comparison is particularly important because the two determinations have minimal overlap in their systematics. That is, the TRGB H_0 value is calibrated via the distance to the LMC²⁵ using the CSP-I sample of SNe Ia, whereas the Cepheid H_0 value, in this particular comparison, is calibrated via the maser in NGC 4528 and Milky Way parallaxes and uses the Supercal distant SN Ia sample. There are no measurements in common between these two methods; therefore, the results are an excellent test of systematics. The independent TRGB and Cepheid results differ at the $\pm 1.7\sigma$ level. However, if one compares the astrophysical methods (by combining the two local measurements, TRGB and Cepheids), treating them as independent measurements, a value of $H_0 = 72.26 \pm 1.19 \text{ km s}^{-1} \text{ Mpc}^{-1}$ is found, resulting in a 3.7σ tension with the Planck results.

We emphasize again that the methods of the TRGB and Cepheids are entirely independent. The RGB stars are an old metal-poor halo population, whereas the Cepheids are a young metal-rich disk population. The physics of the helium flash for red giants and the pulsation mechanism for Cepheids are unrelated. The lines of sight to the SN host galaxies have unrelated dust columns, one through the halo and the other through the gas-rich disk of the parent galaxy. Thus, the quantitative intercomparison of these two methods provides an external test of the level at which systematic errors are independently affecting each of the two methods. For very nearby galaxies ($< 10 \text{ Mpc}$), the agreement is excellent: the scatter in the galaxy-to-galaxy comparison for the TRGB and Cepheid distances in common amounts to only $\pm 0.05 \text{ mag}$, or 2% (see Section 4). The scatter in the galaxy-to-galaxy comparison for the TRGB and Cepheid distances for the

SN Ia host galaxies alone is significantly larger, amounting to $\pm 0.17 \text{ mag}$ (Section 4), and it is larger than what is expected from the published error bars. The scatter in the local Hubble diagram (velocity versus distance) for the TRGB stars is 1.4 times lower than the scatter in the equivalent diagram for the Cepheids, indicating that the TRGB distances are more precise for these larger distances.

The TRGB method has a number of advantages when applied to RGB stars in the halos of galaxies; these include low extinction by dust, low crowding/blending, and a metallicity effect that can be empirically calibrated directly for the TRGB stars themselves. In the I band, there is almost no dependence on metallicity. There is also no need for multiple epochs of observations or concerns of different slopes with period, as in the case of Cepheid variables. In addition, the host masses of our TRGB host-galaxy sample are more massive, on average, than the galaxies in the Cepheid sample, thereby better matching the range of masses of the CSP-I distant sample. The largest systematics in the TRGB distance scale at present are (1) the absolute zero-point (currently set by the distance and the extinction to the LMC), which determines the absolute magnitude of the TRGB, for which we determine $M_I^{\text{TRGB}} = -4.05 \pm 0.04 \text{ mag}$, and (2) the small number of calibrating galaxies giving rise to the error on the mean for the SN Ia calibration.

Ultimately, an unambiguous resolution of the H_0 tension will require a local measurement of H_0 to better than 1%, a goal beyond the reach of current data sets. We note that the TRGB method holds considerable promise for improved accuracy in the near future, as *Gaia* will provide a zero-point calibration to better than 1% accuracy, and the number of calibrators can continue to be increased using both *HST* and *JWST* to bring down the uncertainty in the calibration of SNe Ia to below the 1% level.

We close by reiterating that the new TRGB results do not resolve the current H_0 tension. Stated most simply, they agree

²⁵ We note that the result is unchanged (and the tension insignificantly so) whether or not we include the *Spitzer*-based Cepheid distance modulus to the LMC for the TRGB calibration.

with both the Planck and Cepheid H_0 values. If taken alone, the TRGB results compared to those of Planck would suggest that there is no need for additional physics beyond the current standard cosmological model. However, there is strong motivation for using independent local measurements to test the standard model and its extrapolation to the present day. As noted above, if we combine the TRGB and Cepheid measurements and determine an independent local H_0 value, the tension with Planck is at a 3.7σ level, a significant tension, albeit lower than that seen for the Cepheids alone. Our results suggest that there is more work to be done to reduce systematic errors in the local distance scale before additional physics beyond the standard model is unequivocally called for. Whichever way the tension ultimately resolves, confirming the standard model or pointing the way to additional physics, this issue remains one of the most important in cosmology today.

Support for program No. 13691 was provided by NASA through a grant from the Space Telescope Science Institute, which is operated by the Association of Universities for Research in Astronomy, Inc., under NASA contract NASA 5-26555. The CSP-I has been supported by the National Science Foundation under grants AST 0306969, AST 0607438, AST 1008343, AST 1613426, and AST 1613472. M.G.L. is supported by a grant from the National Research Foundation (NRF) of Korea, funded by the Korean Government (NRF-2017R1A2B4004632). Partial support for this work was provided by NASA through Hubble Fellowship grant No. 51386.01 to R.L.B. by the Space Telescope Science Institute, which is operated by the Association of Universities for Research in Astronomy, Inc., for NASA under contract NAS 5-26555. Computing resources used for this work were made possible by a grant from the Ahmanson Foundation. This research has made use of the NASA/IPAC Extragalactic Database (NED), which is operated by the Jet Propulsion Laboratory, California Institute of Technology, under contract with the National Aeronautics and Space Administration. Some of the data presented in this paper were obtained from the Mikulski Archive for Space Telescopes (MAST). The STScI is operated by the Association of Universities for Research in Astronomy, Inc., under NASA contract NAS 5-26555. We thank the Observatories of the Carnegie Institution for Science and the University of Chicago for their support of our long-term research into the calibration and determination of the expansion rate of the universe. We gratefully acknowledge Vicky Scowcroft for her early contributions to the project. W.L.F. thanks Stanford University for two visits, during which time part of this paper was written. We thank Adam Riess for helpful correspondence concerning the LMC calibration. We also thank the anonymous referee for constructive comments.

Facility: *HST* (ACS).

Appendix A Estimate of Reddening to the LMC TRGB Calibration Sample

For completeness, we briefly describe the method used by B. F. Madore & W. L. Freedman (2019, in preparation) for determining the reddening to the LMC outer-field TRGB stars.

This method employs multiwavelength observations in a similar manner to that which has been widely in use for determining distances and reddenings to Cepheids in nearby

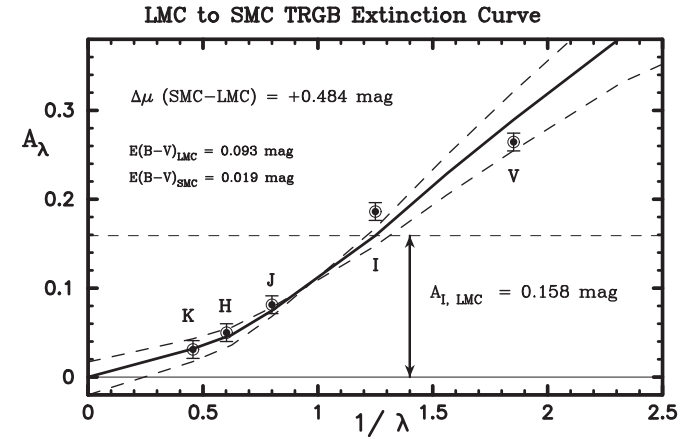


Figure 19. Multiwavelength extinction as a function of inverse wavelength for TRGB stars in the bar of the LMC. Differencing the apparent magnitudes of the TRGB stars in the LMC with respect to those in the SMC, measured at five different wavelengths from the near-infrared (JHK) to the optical (VI), allows one to simultaneously solve for the difference in true distance modulus $\Delta\mu = +0.484$ mag and derive the total line-of-sight reddening to the LMC TRGB stars. In this case, a value of $E(B - V) = +0.093$ mag is obtained. The flanking dashed lines are $\pm 2\sigma$ about the fit. The horizontal dashed line shows the value of A_I .

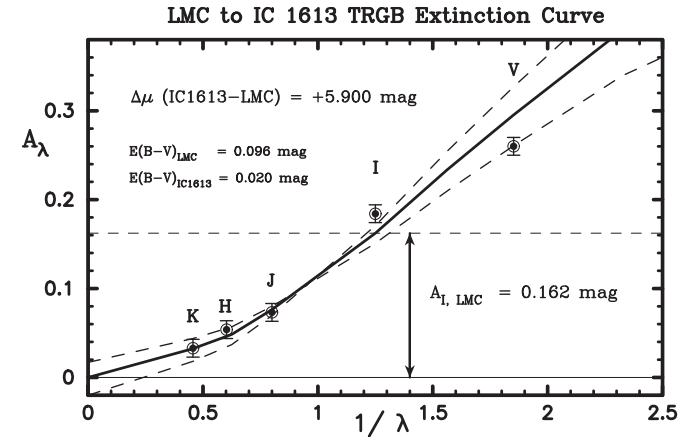


Figure 20. Multiwavelength extinction as a function of inverse wavelength for TRGB stars in the bar of the LMC. Differencing the apparent magnitudes of the TRGB stars in the LMC with respect to those in the dwarf galaxy IC 1613, measured at five different wavelengths from the near-infrared (JHK) to the optical (VI), allows one to simultaneously solve for the difference in true distance modulus $\Delta\mu = +5.900$ mag and derive the total line-of-sight reddening to the LMC TRGB stars. In this case, a value of $E(B - V) = +0.096$ mag is obtained. Dashed lines are the same as in Figure 19.

galaxies. Measurements of the apparent magnitudes of the TRGB at multiple wavelengths are used to derive individual apparent moduli as a function of inverse wavelength; a reddening law can then be fit to these data, giving the total line-of-sight extinction. These methods were first introduced by Freedman et al. (1985) and Freedman (1988), with recent examples being Scowcroft et al. (2013), who used nine-band photometry to study the Cepheids in IC 1613, and Rich et al. (2014), who used seven-band photometry to determine the distances and reddenings to Cepheids in NGC 6822.

In this context, B. F. Madore & W. L. Freedman (2019, in preparation) used the two low-reddening galaxies, IC 1613 and the SMC, as differential calibrators relative to the LMC. Both of these galaxies also have measured apparent magnitudes for their TRGB populations at the same set of wavelengths as the

LMC sample. Differential distance moduli and reddenings can then been obtained with high precision between IC 1613 and the SMC, as well as between them individually and the LMC, as shown in Figures 19 and 20.

The zero-point of the reddening calibration is set using the (low) value of the total line-of-sight extinction of $E(B - V) = 0.02 \pm 0.003$ mag for IC 1613, which was derived from the all-sky reddening maps published by Schlafly & Finkbeiner (2011). The zero-point of the reddening-corrected, absolute magnitude calibration is in turn set at the LMC itself, where the geometric distance modulus of 18.477 ± 0.026 mag has been recently determined by Pietrzynski (2019). The multiwavelength TRGB absolute magnitude calibrations can now be used to determine both distances and reddenings for any future TRGB observations made at three or more wavelengths.

For completeness, these calibrations are given below:

$$M_V = -2.44 + 1.00 \times [(V - I)_o - 1.6]$$

$$M_I = -4.04$$

$$M_J = -5.16 - 0.85 \times [(J - K)_o - 1.0]$$

$$M_H = -5.93 - 1.62 \times [(J - K)_o - 1.0]$$

$$M_K = -6.12 - 1.85 \times [(J - K)_o - 1.0].$$

Appendix B

Flow- and Group-corrected Velocities for Nearby Calibrators

The velocities for the nearby calibrators have been corrected using the linear multi-attractor model available in NED. We provide additional notes below for individual galaxies. Further corrections are made if the galaxy is a member of a group, as noted below.

NGC 3021 is a member of the triple system KTG 26. The average heliocentric velocity of the triple is $+1492 \text{ km s}^{-1}$, and the flow correction applied was $+394 \text{ km s}^{-1}$.

NGC 3370 is the brightest member of a small group. The flow-corrected velocity as listed was averaged over 24 group members.

NGC 4038/39 is an interacting double. The average velocity of the two components from NED was used.

NGC 5584 is a member of the Virgo III association. The average heliocentric velocities of 13 group members is $+1608 \text{ km s}^{-1}$, and the flow correction applied was $+375 \text{ km s}^{-1}$.

M101 is an isolated galaxy whose NED flow-corrected velocity is $+455 \text{ km s}^{-1}$.

NGC 1309 is a member of a small group whose mean flow-corrected velocity is $+1864 \text{ km s}^{-1}$.

NGC 1365 is a member of the Fornax cluster, whose local expansion velocity is taken to be $+1306 \text{ km s}^{-1}$ (Madore et al. 1999).

NGC 1448 is a member of a triplet that has a mean heliocentric velocity of 1142 km s^{-1} and a flow correction of -95 km s^{-1} .

NGC 4424 is a member of the Virgo cluster, whose local expansion velocity is taken to be $+1050 \text{ km s}^{-1}$.

NGC 4526 is a member of the Virgo cluster, whose local expansion velocity is taken to be $+1050 \text{ km s}^{-1}$.

NGC 4536 is a member of the Virgo cluster, whose local expansion velocity is taken to be $+1050 \text{ km s}^{-1}$.

NGC 3627 (M66) is a member of the Leo group, whose local expansion velocity is taken to be $+689 \text{ km s}^{-1}$.

NGC 3368 (M96) is a member of the Leo group, whose local expansion velocity is taken to be $+689 \text{ km s}^{-1}$.

NGC 1316 is a member of the Fornax cluster, whose local expansion velocity is taken to be $+1306 \text{ km s}^{-1}$ (Madore et al. 1999).

NGC 1404 is a member of the Fornax cluster, whose local expansion velocity is taken to be $+1306 \text{ km s}^{-1}$ (Madore et al. 1999).

NGC 1015 is isolated.

NGC 2442 is a member of the NGC 2442 group. The group velocity is from NED.

NGC 3447 is a member of the M96 group, whose mean heliocentric velocity is 1199 km s^{-1} , with a calculated flow correction of $+248 \text{ km s}^{-1}$.

NGC 3972 is a member of the Ursa Minor group (Fouqué et al. 1992).

NGC 3982 is a member of the Ursa Minor group (Fouqué et al. 1992).

NGC 4639 is a member of the Virgo cluster, whose local expansion velocity is taken to be $+1050 \text{ km s}^{-1}$.

NGC 5917 is a member of an interacting pair, whose mean heliocentric velocity is $+1921 \text{ km s}^{-1}$, with a calculated flow correction of $+323 \text{ km s}^{-1}$.

NGC 7250 is isolated.

UGC 09391 is isolated.

ORCID iDs

Wendy L. Freedman <https://orcid.org/0000-0003-3431-9135>

Barry F. Madore <https://orcid.org/0000-0002-1576-1676>

Dylan Hatt <https://orcid.org/0000-0003-2767-2379>

Taylor J. Hoyt <https://orcid.org/0000-0001-9664-0560>

In Sung Jang <https://orcid.org/0000-0002-2502-0070>

Rachael L. Beaton <https://orcid.org/0000-0002-1691-8217>

Christopher R. Burns <https://orcid.org/0000-0003-4625-6629>

Myung Gyoong Lee <https://orcid.org/0000-0003-2713-6744>

Jillian R. Neeley <https://orcid.org/0000-0002-8894-836X>

M. M. Phillips <https://orcid.org/0000-0003-2734-0796>

Jeffrey A. Rich <https://orcid.org/0000-0002-5807-5078>

Mark Seibert <https://orcid.org/0000-0002-1143-5515>

References

- Abbott, B. P., Abbott, R., Abbott, T. D., et al. 2017, *Natur*, **551**, 85
- Adhikari, S., & Huterer, D. 2019, arXiv:[1905.02278](https://arxiv.org/abs/1905.02278)
- Agrawal, P., Cyr-Racine, F.-Y., Pinner, D., & Randall, L. 2019, arXiv:[1904.01016](https://arxiv.org/abs/1904.01016)
- Alam, S., Ata, M., Bailey, S., et al. 2017, *MNRAS*, **470**, 2617
- Anand, G. S., Tully, R. B., Rizzi, L., & Karachentsev, I. D. 2019, arXiv:[1901.05981](https://arxiv.org/abs/1901.05981)
- Arenou, F., Luri, X., Babusiaux, C., et al. 2018, *A&A*, **616**, A17
- Aubourg, É., Bailey, S., Bautista, J. E., et al. 2015, *PhRvD*, **92**, 123516
- Baade, W. 1944, *ApJ*, **100**, 137
- Beaton, R. L., Freedman, W. L., Madore, B. F., et al. 2016, *ApJ*, **832**, 210
- Beaton, R. L., Seibert, M., Hatt, D., et al. 2019, *ApJ*, submitted
- Bellazzini, M., Ferraro, F. R., & Pancino, E. 2001, *ApJ*, **556**, 635
- Benedict, G. F., McArthur, B. E., Feast, M. W., et al. 2007, *AJ*, **133**, 1810
- Bennett, C. L., Larson, D., Weiland, J. L., et al. 2013, *ApJS*, **208**, 20
- Bernal, J. L., Verde, L., & Riess, A. G. 2016, *JCAP*, **10**, 019
- Betoule, M., Kessler, R., Guy, J., et al. 2014, *A&A*, **568**, A22
- Bildsten, L., Paxton, B., Moore, K., & Macias, P. J. 2012, *ApJL*, **744**, L6
- Birrer, S., Treu, T., Rusu, C. E., et al. 2018, arXiv:[1809.01274](https://arxiv.org/abs/1809.01274)
- Burns, C. R., Parent, E., Phillips, M. M., et al. 2018, arXiv:[1809.06381](https://arxiv.org/abs/1809.06381)

- Burns, C. R., Stritzinger, M., Phillips, M. M., et al. 2011, *AJ*, **141**, 19
 Burns, C. R., Stritzinger, M., Phillips, M. M., et al. 2014, *ApJ*, **789**, 32
 Caldwell, R. R., & Kamionkowski, M. 2004, *JCAP*, **9**, 009
 Cardelli, J. A., Clayton, G. C., & Mathis, J. S. 1989, *ApJ*, **345**, 245
 Cartier, R., Hamuy, M., Pignata, G., et al. 2014, *ApJ*, **789**, 89
 Cassisi, S., & Salaris, M. 2013, Old Stellar Populations: How to Study the Fossil Record of Galaxy Formation (New York: Wiley)
 Chen, H.-Y., Fishbach, M., & Holz, D. E. 2018, *Natur*, **562**, 545
 Childress, M., Aldering, G., Antilogus, P., et al. 2013, *ApJ*, **770**, 108
 Cioni, M.-R. L., van der Marel, R. P., Loup, C., & Habing, H. J. 2000, *A&A*, **359**, 601
 Cole, S., Percival, W. J., Peacock, J. A., et al. 2005, *MNRAS*, **362**, 505
 Contreras, C., Hamuy, M., Phillips, M. M., et al. 2010, *AJ*, **139**, 519
 D'Arcy Kenworthy, W., Scolnic, D., & Riess, A. 2019, arXiv:1901.08681
 Efstathiou, G. 2014, *MNRAS*, **440**, 1138
 Eisenstein, D. J., Zehavi, I., Hogg, D. W., et al. 2005, *ApJ*, **633**, 560
 Elias, J. H., Frogel, J. A., Hackwell, J. A., & Persson, S. E. 1981, *ApJL*, **251**, L13
 Feeney, S. M., Mortlock, D. J., & Dalmasso, N. 2017, arXiv:1707.00007
 Ferrarese, L., Mould, J. R., Kennicutt, R. C., Jr., et al. 2000, *ApJ*, **529**, 745
 Fitzpatrick, E. L. 1999, *PASP*, **111**, 63
 Folatelli, G., Morrell, N., Phillips, M. M., et al. 2013, *ApJ*, **773**, 53
 Follin, B., & Knox, L. 2017, arXiv:1707.01175
 Fouqué, P., Gourgoulhon, E., Chamaraux, P., & Paturel, G. 1992, *A&AS*, **93**, 211
 Freedman, W. 2014, CHP-II: The Carnegie Hubble Program to Measure H_0 to 3% Using Population II, HST Proposal ID, **13691**
 Freedman, W. L. 1988, *ApJ*, **326**, 691
 Freedman, W. L. 2017, *NatAs*, **1**, 0169
 Freedman, W. L., Burns, C. R., Phillips, M. M., et al. 2009, *ApJ*, **704**, 1036
 Freedman, W. L., Grieve, G. R., & Madore, B. F. 1985, *ApJS*, **59**, 311
 Freedman, W. L., & Madore, B. F. 1990, *ApJ*, **365**, 186
 Freedman, W. L., & Madore, B. F. 2010, *ARA&A*, **48**, 673
 Freedman, W. L., Madore, B. F., Gibson, B. K., et al. 2001, *ApJ*, **553**, 47
 Freedman, W. L., Madore, B. F., Scowcroft, V., et al. 2012, *ApJ*, **758**, 24
 Frieman, J. A. 1996, *ComAp*, **18**, 323
 Gall, C., Stritzinger, M. D., Ashall, C., et al. 2018, *A&A*, **611**, A58
 Graziani, R., Courtois, H. M., Lavaux, G., et al. 2019, *MNRAS*, in press
 Hamuy, M., Folatelli, G., Morrell, N. I., et al. 2006, *PASP*, **118**, 2
 Hamuy, M., Phillips, M. M., Maza, J., et al. 1991, *AJ*, **102**, 208
 Haschke, R., Grebel, E. K., & Duffau, S. 2011, *AJ*, **141**, 158
 Hatt, D., Beaton, R. L., Freedman, W. L., et al. 2017, *ApJ*, **845**, 146
 Hatt, D., Freedman, W. L., Madore, B. F., et al. 2018a, *ApJ*, **861**, 104
 Hatt, D., Freedman, W. L., Madore, B. F., et al. 2018b, *ApJ*, **866**, 145
 Herrnstein, J. R., Moran, J. M., Greenhill, L. J., et al. 1999, *Natur*, **400**, 539
 Holz, D. E. 1998, *ApJL*, **506**, L1
 Hoscheit, B. L., & Barger, A. J. 2018, *ApJ*, **854**, 46
 Hoyle, F., & Fowler, W. A. 1960, *ApJ*, **132**, 565
 Hoyt, T. J., Freedman, W. L., Barry, F., et al. 2019, *ApJ*, in press
 Hoyt, T. J., Freedman, W. L., Madore, B. F., et al. 2018, *ApJ*, **858**, 12
 Humphreys, E. M. L., Reid, M. J., Moran, J. M., Greenhill, L. J., & Argon, A. L. 2013, *ApJ*, **775**, 13
 Jang, I. S., Hatt, D., Beaton, R. L., et al. 2018, *ApJ*, **852**, 60
 Jang, I. S., & Lee, M. G. 2015, *ApJ*, **807**, 133
 Jang, I. S., & Lee, M. G. 2017a, *ApJ*, **836**, 74
 Jang, I. S., & Lee, M. G. 2017b, *ApJ*, **835**, 28
 Jha, S., Garnavich, P. M., Kirshner, R. P., et al. 1999, *ApJS*, **125**, 73
 Joshi, Y. C., & Panchal, A. 2019, arXiv:1906.04481
 Karachentsev, I. D., Grebel, E. K., Sharina, M. E., et al. 2003, *A&A*, **404**, 93
 Karachentsev, I. D., Makarova, L. N., Tully, R. B., Rizzi, L., & Shaya, E. J. 2018, *ApJ*, **858**, 62
 Karwal, T., & Kamionkowski, M. 2016, *PhRvD*, **94**, 103523
 Kelly, P. L., Hicken, M., Burke, D. L., Mandel, K. S., & Kirshner, R. P. 2010, *ApJ*, **715**, 743
 Krisciunas, K., Contreras, C., Burns, C. R., et al. 2017, *AJ*, **154**, 211
 Krisciunas, K., Suntzeff, N. B., Candia, P., et al. 2003, *AJ*, **125**, 166
 Krist, J. E., Hook, R. N., & Stoehr, F. 2011, *Proc. SPIE*, **8127**, 81270J
 Lampeitl, H., Smith, M., Nichol, R. C., et al. 2010, *ApJ*, **722**, 566
 Lee, M. G., Freedman, W. L., & Madore, B. F. 1993, *ApJ*, **417**, 553
 Lindegren, L., Hernández, J., Bombrun, A., et al. 2018, *A&A*, **616**, A2
 Livio, M., & Mazzali, P. 2018, *PhR*, **736**, 1
 Macaulay, E., Nichol, R. C., Bacon, D., et al. 2018, arXiv:1811.02376
 Madore, B. F. 1982, *ApJ*, **253**, 575
 Madore, B. F., & Freedman, W. L. 1991, *PASP*, **103**, 933
 Madore, B. F., & Freedman, W. L. 1995, *AJ*, **109**, 1645
 Madore, B. F., & Freedman, W. L. 1999, in ASP Conf. Ser. 167, Harmonizing Cosmic Distance Scales in a Post-HIPPARCOS Era, ed. D. Egret & A. Heck (San Francisco, CA: ASP), **161**
 Madore, B. F., Freedman, W. L., Hatt, D., et al. 2018, *ApJ*, **858**, 11
 Madore, B. F., Freedman, W. L., Silbermann, N., et al. 1999, *ApJ*, **515**, 29
 Madore, B. F., Mager, V., & Freedman, W. L. 2009, *ApJ*, **690**, 389
 Mager, V. A., Madore, B. F., & Freedman, W. L. 2008, *ApJ*, **689**, 721
 Mandel, K. S., Narayan, G., & Kirshner, R. P. 2011, *ApJ*, **731**, 120
 Mandel, K. S., Scolnic, D. M., Shariff, H., Foley, R. J., & Kirshner, R. P. 2017, *ApJ*, **842**, 93
 Marion, G. H., Brown, P. J., Vinkó, J., et al. 2016, *ApJ*, **820**, 92
 Matheson, T., Joyce, R. R., Allen, L. E., et al. 2012, *ApJ*, **754**, 19
 McGonegal, R., McAlary, C. W., Madore, B. F., & McLaren, R. A. 1982, *ApJL*, **257**, L33
 Méndez, B., Davis, M., Moustakas, J., et al. 2002, *AJ*, **124**, 213
 Monson, A. J., Beaton, R. L., Scowcroft, V., et al. 2017, *AJ*, **153**, 96
 Monson, A. J., Freedman, W. L., Madore, B. F., et al. 2012, *ApJ*, **759**, 146
 Mörtzell, E., & Dhawan, S. 2018, *JCAP*, **9**, 025
 Mould, J., Clementini, G., & Da Costa, G. 2019, *PASA*, **36**, e001
 Mould, J., & Kristian, J. 1986, *ApJ*, **305**, 591
 Mould, J., & Sakai, S. 2008, *ApJL*, **686**, L75
 Mould, J. R., Huchra, J. P., Freedman, W. L., et al. 2000, *ApJ*, **529**, 786
 Nataf, D. M. 2015, *MNRAS*, **449**, 1171
 Ngeow, C.-C., & Kanbur, S. M. 2005, *MNRAS*, **360**, 1033
 Ngeow, C.-C., Kanbur, S. M., Nikolaev, S., et al. 2005, *MNRAS*, **363**, 831
 Perlmutter, S., Aldering, G., Goldhaber, G., et al. 1999, *ApJ*, **517**, 565
 Persson, S. E., Madore, B. F., Krzeminski, W., et al. 2004, *AJ*, **128**, 2239
 Phillips, M. M. 1993, *ApJL*, **413**, L105
 Pietrzynski, G. 2019, *Natur*, **567**, 200
 Pietrzynski, G., Graczyk, D., Gieren, W., et al. 2013, *Natur*, **495**, 76
 Planck Collaboration, Ade, P. A. R., Aghanim, N., et al. 2016, *A&A*, **594**, A13
 Planck Collaboration, Aghanim, N., Akrami, Y., et al. 2018, arXiv:1807.06209
 Poulin, V., Smith, T. L., Karwal, T., & Kamionkowski, M. 2018, arXiv:1811.04083
 Rich, J. A., Persson, S. E., Freedman, W. L., et al. 2014, *ApJ*, **794**, 107
 Richmond, M. W., & Smith, H. A. 2012, *JAVSO*, **40**, 872
 Richmond, M. W., Treffers, R. R., Filippenko, A. V., et al. 1995, *AJ*, **109**, 2121
 Riess, A. G., Casertano, S., Yuan, W., Macri, L. M., & Scolnic, D. 2019, *ApJ*, **876**, 85
 Riess, A. G., Filippenko, A. V., Challis, P., et al. 1998, *AJ*, **116**, 1009
 Riess, A. G., Kirshner, R. P., Schmidt, B. P., et al. 1999, *AJ*, **117**, 707
 Riess, A. G., Li, W., Stetson, P. B., et al. 2005, *ApJ*, **627**, 579
 Riess, A. G., Macri, L., Casertano, S., et al. 2011, *ApJ*, **730**, 119
 Riess, A. G., Macri, L. M., Hoffmann, S. L., et al. 2016, *ApJ*, **826**, 56
 Rigault, M., Aldering, G., Kowalski, M., et al. 2015, *ApJ*, **802**, 20
 Rizzi, L., Tully, R. B., Makarov, D., et al. 2007, *ApJ*, **661**, 815
 Russ, J. C. 1992, The Image Processing Handbook (Boca Raton, FL: CRC Press)
 Sakai, S., Madore, B. F., & Freedman, W. L. 1996, *ApJ*, **461**, 713
 Salaris, M., & Cassisi, S. 1997, *MNRAS*, **289**, 406
 Salaris, M., & Cassisi, S. 1998, *MNRAS*, **298**, 166
 Sandage, A., Tamman, G. A., Saha, A., et al. 2006, *ApJ*, **653**, 843
 Saviane, I., Hibbard, J. E., & Rich, R. M. 2004, *AJ*, **127**, 660
 Saviane, I., Momany, Y., da Costa, G. S., Rich, R. M., & Hibbard, J. E. 2008, *ApJ*, **678**, 179
 Schlafly, E. F., & Finkbeiner, D. P. 2011, *ApJ*, **737**, 103
 Schweizer, F., Burns, C. R., Madore, B. F., et al. 2008, *AJ*, **136**, 1482
 Scolnic, D., Casertano, S., Riess, A., et al. 2015, *ApJ*, **815**, 117
 Scolnic, D. M., Jones, D. O., Rest, A., et al. 2018, *ApJ*, **859**, 101
 Scowcroft, V., Freedman, W. L., Madore, B. F., et al. 2011, *ApJ*, **743**, 76
 Scowcroft, V., Freedman, W. L., Madore, B. F., et al. 2013, *ApJ*, **773**, 106
 Serenelli, A., Weiss, A., Cassisi, S., Salaris, M., & Pietrinferni, A. 2017, *A&A*, **606**, A33
 Shafieloo, A., Keeley, R. E., & Linder, E. V. 2018, arXiv:1812.07775
 Shapley, H. 1918, *ApJ*, **48**, 89
 Silverman, J. M., Foley, R. J., Filippenko, A. V., et al. 2012, *MNRAS*, **425**, 1789
 Smith, M., Bacon, D. J., Nichol, R. C., et al. 2014, *ApJ*, **780**, 24
 Sorce, J. G., Courtois, H. M., Tully, R. B., et al. 2013, *ApJ*, **765**, 94
 Stetson, P. B. 1987, *PASP*, **99**, 191
 Stetson, P. B. 1994, *PASP*, **106**, 250
 Stritzinger, M., Burns, C. R., Phillips, M. M., et al. 2010, *AJ*, **140**, 2036
 Stritzinger, M. D., Phillips, M. M., Boldt, L. N., et al. 2011, *AJ*, **142**, 156
 Sullivan, M., Conley, A., Howell, D. A., et al. 2010, *MNRAS*, **406**, 782
 Suyu, S. H., Bonvin, V., Courbin, F., et al. 2017, *MNRAS*, **468**, 2590
 Tikhonov, N. A., & Galazutdinova, O. A. 2018, *AstBu*, **73**, 279

- Tripp, R. 1998, *A&A*, **331**, 815
Tsvetkov, D. Y. 1982, *SVAL*, **8**, 115
Tully, R. B., Courtois, H. M., Dolphin, A. E., et al. 2013, *AJ*, **146**, 86
Tully, R. B., Libeskind, N. I., Karachentsev, I. D., et al. 2015, *ApJL*, **802**, L25
Uddin, S. A., Mould, J., Lidman, C., Ruhmann-Kleider, V., & Zhang, B. R. 2017, *ApJ*, **848**, 56
Ulaczyk, K., Szymański, M. K., Udalski, A., et al. 2012, *AcA*, **62**, 247
Visser, M. 2004, *CQGra*, **21**, 2603
Walker, W. S. G., & Marino, B. F. 1982, *PVSS*, **10**, 53
Wells, L. A., Phillips, M. M., Suntzeff, B., et al. 1994, *AJ*, **108**, 2233
Wheeler, J. C., & Hansen, C. J. 1971, *Ap&SS*, **11**, 373
Wu, H.-Y., & Huterer, D. 2017, *MNRAS*, **471**, 4946
Wu, P.-F., Tully, R. B., Rizzi, L., et al. 2014, *AJ*, **148**, 7
Zaritsky, D., Harris, J., Thompson, I. B., & Grebel, E. K. 2004, *AJ*, **128**, 1606
Zaritsky, D., Harris, J., Thompson, I. B., Grebel, E. K., & Massey, P. 2002, *AJ*, **123**, 855
Zhang, B. R., Childress, M. J., Davis, T. M., et al. 2017, *MNRAS*, **471**, 2254